

Learning a phenomenological theory for contact-interactions between motile cells from collision experiments

Tom Brandstätter^{1,2,†}, Emily Brieger^{3,†}, David B. Brückner⁴, Georg Ladurner^{3,5}, Joachim Rädler³, Chase P. Broedersz^{1,2,*}

¹Department of Physics and Astronomy, Vrije Universiteit Amsterdam, De Boelelaan 1105, 1081 HV Amsterdam, The Netherlands.

²Arnold-Sommerfeld-Center for Theoretical Physics, Ludwig-Maximilians-Universität München, Theresienstr. 37, 80333 Munich, Germany.

³Faculty of Physics and Center for NanoScience, Ludwig-Maximilians-Universität München, Geschwister-Scholl-Platz 1, 80539 Munich, Germany.

⁴Institute of Science and Technology Austria, Am Campus 1, 3400 Klosterneuburg, Austria.

⁵Center for Medical Physics and Biomedical Engineering, Währinger Gürtel 18-20, 1090 Wien, Austria.

† These authors contributed equally to this work: Tom Brandstätter, Emily Brieger

* Corresponding author: c.p.broedersz@vu.nl, Phone: +31 20 59 82953

Abstract

The migration behavior of colliding cells is critically determined by transient contact-interactions. During these interactions, the motility machinery, including the front-rear polarization of the cell, dynamically responds to surface protein-mediated transmission of forces and biochemical signals between cells. While biomolecular details of such contact-interactions are increasingly well understood, it remains unclear what biophysical interaction mechanisms govern the cell-level dynamics of colliding cells and how these mechanisms vary across cell types. Here, we develop a phenomenological theory based on eleven candidate contact-interaction mechanisms coupling cell position, shape, and polarity. Using high-throughput micropattern experiments, we detect which of these phenomenological contact-interactions captures the interaction behaviors of cells. We find that various cell types - ranging from mesenchymal to epithelial cells - are accurately captured by a single model with only two interaction mechanisms: polarity-protrusion coupling and polarity-polarity coupling. The qualitatively different interaction behaviors of distinct cells, as well as cells subject to molecular perturbations of surface protein-mediated signaling, can all be quantitatively captured by varying the strength and sign of the polarity-polarity coupling mechanism. Altogether, our data-driven phenomenological theory of cell-cell interactions reveals polarity-polarity coupling as a versatile and general contact-interaction mechanism, which may underlie diverse collective migration behavior of motile cells.

Introduction

Contact-interactions between cells control the coordinated migration of tissues¹ during fundamental physiological processes² in development³, health⁴, and disease⁵. Already at the level of two motile cells, contact-interactions can lead to dramatic changes in the trajectories of cells after they collide⁶⁻⁹. Such interaction behavior is not merely the result of physical forces arising, for example, from membrane adhesion or deformations of the colliding cells. Instead, contact-interactions trigger a dynamical response in the intracellular biomolecular cell motility machinery¹⁰⁻¹². This machinery involves establishing a front-rear polarization^{13,14}, as well as active cytoskeleton contraction and protrusion formation, enabling cells to self-propel¹⁵. Contact-interactions can modify cell polarity via biochemical signaling between cells^{10,16}, reflecting the active, responsive, and adaptive nature of cell motility and cell-cell interactions. Revealing the dominant interaction mechanisms that steer cell polarity and cell migration in response to cell-cell contacts is critical for a general understanding of the dynamics of interacting cells.

The interaction behavior of migrating cells in various processes is highly diverse. During wound healing⁴, for instance, motile epithelial cells follow each other after making contact^{17,18}. By contrast, several developmental processes rely on cells retreating from each other after forming cell-cell contacts¹⁹⁻²², termed Contact Inhibition of Locomotion (CIL)^{7,23}. Many details of the biomolecular machinery underlying these and other interaction behaviors^{24,25} are now becoming increasingly clear. For instance, force transmission between epithelial cells is enabled by E-Cadherin mediated junctions^{26,27}, while receptor-ligand Eph-ephrin interactions^{16,22,28-30} enable cell-cell recognition during CIL. Both of these surface proteins enable cells to regulate their polarity machinery in response to cell-cell contacts^{12,30,31}. Such molecular pathways vary between different cell types and can change, for instance, during the epithelial-to-mesenchymal transition (EMT)^{32,33}. However, it remains a major challenge to understand how contact-interactions vary across different cell types and how they are controlled by the molecular machinery of cells.

The complexity of the motility and cell-cell interaction machinery makes it difficult to gain mechanistic understanding of contact-interactions. Nevertheless, biophysical models can give mechanistic insight into single cell motility^{15,34-37} and how force transmission and cell-cell recognition give rise to the dynamics of interacting cells^{6,38,47-51,39-46}. However, these bottom-up models are commonly tailored to understand specific cell types in concrete settings, making it difficult to achieve a unifying conceptual understanding of contact-interactions. Furthermore, biophysical models for contact-interactions are rarely systematically constrained on quantitative experimental data⁵². High-throughput experimental micropattern assays provide quantitative statistical studies of cell-cell interactions^{9,41,51-53}. These experiments enable data-driven inference approaches to identify effective dynamical descriptions of migrating and interacting cells^{9,52,54,55}. However, data-driven inference neither yields generalizable models nor readily reveals underlying interaction mechanisms. Thus, it remains an open challenge to develop a broadly applicable biophysical theory for contact-interactions.

Phenomenological model for contact-interactions

Here, we develop a phenomenological dynamical theory that quantitatively describes how the motion of migrating cells responds to contact-interactions. We employ a minimal large-scale description where the cell's nucleus position $\mathbf{x}_n(t)$ and the leading protrusion position $\mathbf{x}_p(t)$ are the relevant positional degrees of freedom of a migrating cell (Fig. 1a). This simple choice captures the cell's position, as well as the elongated and dynamic shape of migrating cells observed widely in single-cell^{34,56} and cell-cell interaction⁶⁻⁹ experiments. To complete our description, we include an internal degree of freedom $\mathbf{P}(t)$ to capture cell polarity. This polarity describes the cell's anisotropic organization of the cytoskeletal motility machinery, distinguishing front and rear¹³. This minimal level of description has proven adequate to describe single cell migration^{34,35}, thereby providing a foundation to develop a general theory for how contact-interactions determine cell shape, polarity, and the dynamics of migrating cells.

We define the dynamics of interacting cells by equations of motion for the positional degrees of freedom together with a stochastic description of cell polarity. For simplicity, we consider interaction behavior of cells in 1D, and write for cell i :

$$\dot{x}_{n,i} = F_n(x_{n,i}, x_{p,i}) + G_n(\Delta x, P, \Delta P) \quad (1)$$

$$\dot{x}_{p,i} = F_p(x_{n,i}, x_{p,i}) + P_i(t) + G_p(\Delta x, P, \Delta P) \quad (2)$$

$$\dot{P}_i = F_P(x_{p,i}, P_i) + G_P(\Delta x, P, \Delta P) + \sigma \eta_i(t). \quad (3)$$

Here, the polarity drives the protrusion⁵⁷ and the functions F_n , F_p , and F_P are one-body terms describing the single-cell behavior including a mechanical coupling between nucleus and protrusion, as well as a response of the cells to their micro-environment³⁴ (Methods). These single-cell terms can be derived from a microscopic theory of cell migration^{14,35,37} and are constrained by experimental data of single migrating cells³⁴. In this model, stochasticity arises in the polarity dynamics, which includes Gaussian white noise $\eta_i(t)$ with amplitude σ .

Cell-cell interaction mechanisms are captured by two-body terms G_n , G_p , and G_P that may depend on the intercellular distances Δx , cell polarities P , and polarity differences ΔP . Deriving these terms rigorously from detailed biophysical and biochemical signaling processes and mechanical coupling between cells is currently unfeasible. Therefore, we employ a phenomenological approach: In an unbiased way, we propose a set of 21 possible candidate cell-cell interaction mechanisms arising from the lowest-order linear couplings of the degrees of freedom allowed by rotational and translational symmetry (Fig. 1b), as described in more detail later on (Fig. 4). In principle, all candidate cell-cell interaction mechanisms may contribute to the behavior of interacting cells. Additionally, distinct cell types may exhibit different cell-cell interactions, further exacerbating the challenge to reveal the cell-cell interaction mechanisms underlying behavior. Therefore, we require strong quantitative model constraints from experiments to discover what interaction mechanisms are relevant to describe interaction behavior across a broad range of cell types.

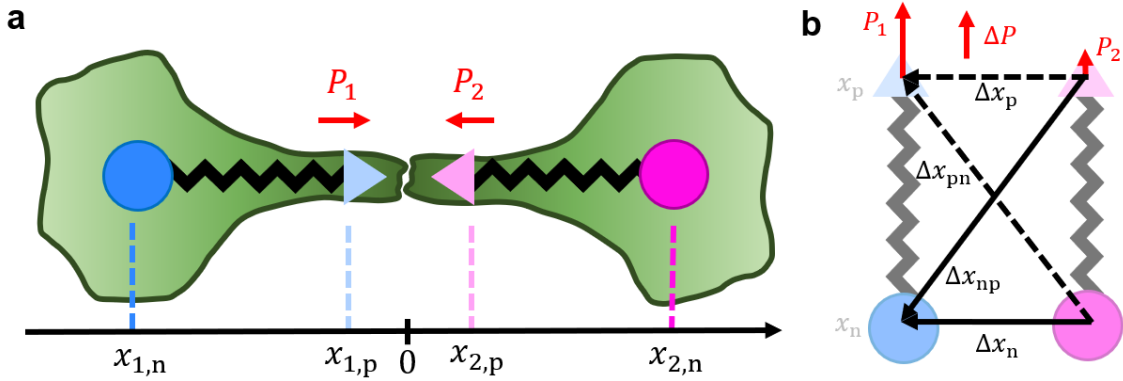


Figure 1 | A phenomenological model for contact-interactions. **a)** To describe the interaction behavior of a whole cell, we include three dynamical degrees of freedom in our model: the position of the nucleus x_n , the position of the protrusion x_p , and the polarity of a cell P . The polarity determines a self-propulsion force, giving rise to cell migration (Methods). **b)** Schematic representation of all linear and vectorial couplings between cell 1 and cell 2.

Cell-cell collision experiments reveal diversity of interaction behaviors

To detect contact-interactions in experiments, we use a high-throughput assay to study the dynamics of homotypic pairs of interacting motile cells. Specifically, we employ a dumbbell-shaped micropattern as a minimal cell collider⁹ (Fig. 2c). This geometry effectively confines cells in 1D, isolates cell pairs, and generates many cell-cell collision events. To capture a variety of cell-cell interactions across cell types in parallel, we consider a range of distinct motile cells from human tissue. We study the two metastatic breast cancer cell lines MDA-MB-231 and MDA-MB-436, the fibrosarcoma cell line HT-1080, the non-metastatic lung cancer cell line A549, and the epithelial non-cancerous breast cell line MCF10A (Fig. 2a). These cell lines express different levels of adhesion proteins and exhibit distinct collective behaviors *in vitro*: MDA-MB-231 cells neither express the cell adhesion molecule E-cadherin nor N-Cadherin (Fig. 2b), and do not form monolayers (Fig. 2a i). The breast cancer cells MDA-MB-436 and fibrosarcoma cells express N-Cadherin (Fig. 2b ii) and also do not form monolayers (Fig. 2a ii,iii). These features are characteristic of a mesenchymal phenotype⁵⁸. In contrast, MCF10A and A549 cells express E-cadherin (Fig. 2b i) and form monolayers (Fig. 2a iv,v), characteristic of an epithelial phenotype⁵⁸. All tested cell lines are motile on our micropattern and repeatedly collide with each other (Fig. 2d, Supplementary movie 1). However, the collision behavior of cells is variable with marked differences across the five cell lines. To quantify the behavior of pairs of colliding cells in our experiments, we use a low-dimensional representation of these interaction dynamics by tracking the 1D motion of the nucleus of both cells over time (Fig. 2e). This approach yields a large ensemble of experimental trajectory data reflecting the cell-level dynamics of interacting cells.

We start by characterizing distinct cell types using various interaction behavior statistics⁹. First, we quantify how cells coordinate their behaviors in close proximity using a velocity cross-correlation function of two cells occupying the same island: $C_V(|t - t'|) = \langle v_1(t)v_2(t') \rangle_{\text{same}}$ (Methods). The breast cancer and fibrosarcoma cell lines exhibit negative or

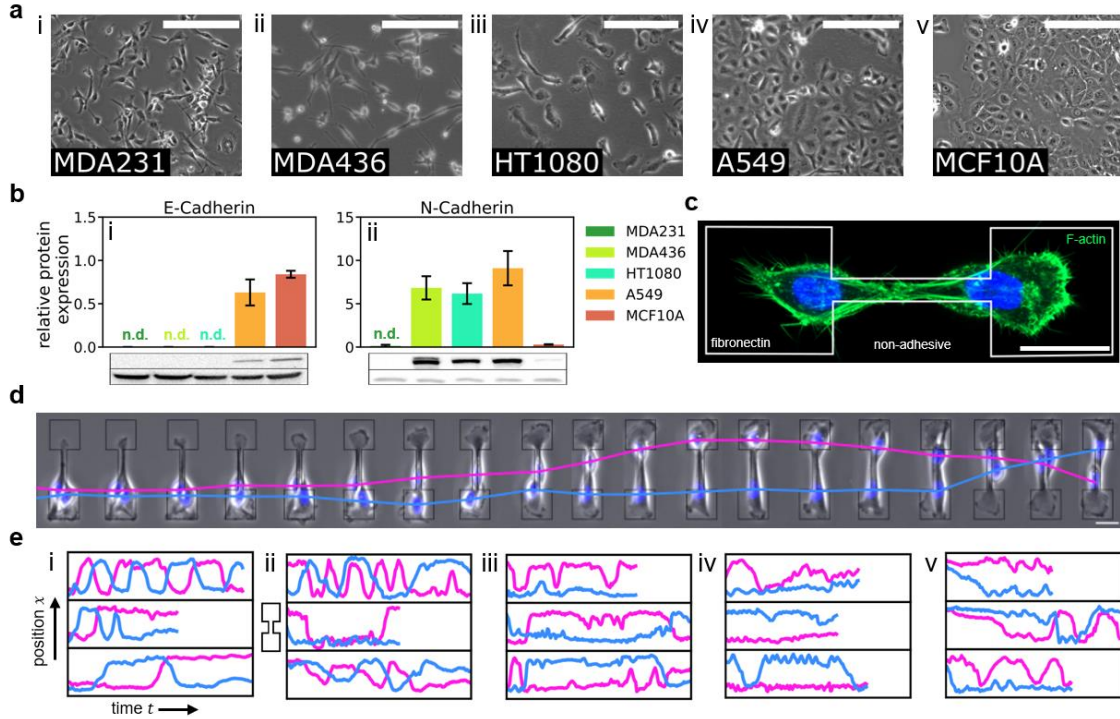


Figure 2 | Studying transient cell collisions on a minimal cell collider. **a**) Brightfield microscopy images of (i) MDA-MB-231 cells, (ii) MDA-MB-436 cells, (iii) HT1080 cells, (iv) A549 cells and (v) MCF10A cells under *in vitro* conditions. Scale bar: 200 μm . **b**) Quantitative western blot analysis of protein expression levels of E-Cadherin and N-Cadherin in the different cell lines. We show one blot for each protein with its corresponding loading control (β -actin) (Methods). Error bars indicate the error of the mean (s.e.m) of triplicate measurements. **c**) Two migrating MCF10A cells (F-actin stained in green, nucleus in blue) are confined on a dumbbell-shaped micropattern (white outline), which consists of two islands connected by a bridge. The micropattern is coated with fibronectin and is surrounded by a non-adhesive PLL-PEG layer. **d**) Time series of brightfield images of two MDA-MB-231 cells colliding repeatedly while hopping between the islands. Scale bar in both c) and d): 25 μm . **e**) Small selection of nucleus trajectories for the five different cell lines.

very small instantaneous velocity correlations, while the epithelial cells exhibit positive instantaneous velocity correlations (Fig. 3a). Furthermore, we determine a position correlation function $C_X(|t - t'|) = \langle x_1(t)x_2(t') \rangle$. All cell types exhibit negative instantaneous position correlations (Fig. 3b), indicating mutual exclusion. To gain insight into how cells navigate each other on longer time scales, we analyze cell-cell collisions⁹. We detect sliding events (two cells interchange positions), reversal events (at least one cell retracts) and following events (both cells transition simultaneously) (Methods). The two breast cancer cell lines mostly exhibit sliding behavior, while the epithelial and fibrosarcoma cells mostly exhibit reversal behavior (solid bars Fig. 3c). Altogether, these results show different dominant interaction behaviors across our cell types with marked differences between epithelial and cancer cell lines.

Data-driven inference constrains cell-cell interactions

To further guide the development of a phenomenological model for cell-cell interactions, we investigate the effective short-time dynamics of the nucleus. Specifically, we employ a data-driven inference approach to learn interacting stochastic equations of motion from the

experimentally measured cell position x and cell velocity v ^{52,56}. In contrast to the general phenomenological model in Eqs. (1-3), such equations of motion are underdamped, implicitly capturing the effective inertia of cell polarity³⁴. For pairs of cells^{9,52}, we assume coupled Langevin equations of the form:

$$\frac{dv_i}{dt} = F(x_i, v_i) + f(\Delta x)\Delta x + \gamma(\Delta x)\Delta v + \sigma\eta(t). \quad (4)$$

Here, $F(x_i, v_i)$ describes single cell behavior and interaction with the confining geometry, and $\sigma\eta(t)$ represents a Gaussian white noise with amplitude σ . Of particular importance here are the interaction terms $f(\Delta x)\Delta x$ and $\gamma(\Delta x)\Delta v$, which capture how the cell nuclei deterministically accelerate depending on the cells' relative separation Δx and velocity Δv . The functions $f(\Delta x)$ and $\gamma(\Delta x)$ encode the sign and spatial structure of the interactions and are inferred from experimental data. Here, $f(\Delta x)\Delta x > 0$ implies effective repulsion, while negative values indicate effective attraction. In contrast, $\gamma(\Delta x) < 0$ indicates effective cell-cell friction, while positive values indicate effective anti-friction. Our goal is to connect these inferred dynamical terms to the interpretable interactions of our phenomenological model (Eqs. 1-3) (Fig. 3d).

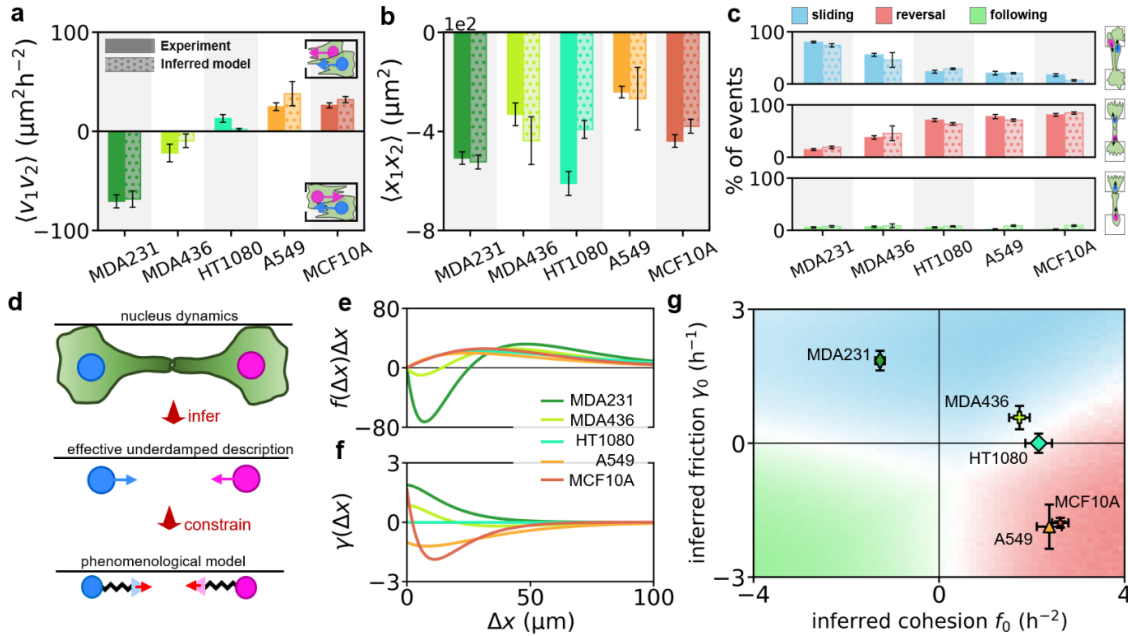


Figure 3 | Quantifying interaction behavior using data-driven inference. **a)** Instantaneous velocity cross-correlation $C_V(|t - t'| = 0)$ between the two cells when they occupy the same island. Solid bars show experimental results, dotted bars show the prediction of the inferred underdamped description. For panels (a)-(c), error bars show the error of the mean (s.e.m) obtained from bootstrapping the experimental data. **b)** Instantaneous position cross-correlation $C_X(|t - t'| = 0)$. **c)** Percentages of the different collision events for the different cell lines. **d)** Schematic of our modelling strategy. **e)** Inferred cohesion interactions $f(\Delta x)\Delta x$ for the five different cell lines. **f)** Inferred friction interactions $\gamma(\Delta x)\Delta v$ of the various cell lines. **g)** Interaction behavior space spanned by the amplitudes of the inferred cohesion and friction interactions, f_0 and γ_0 . Colors show the dominant collision event predicted in that parameter region. Throughout this figure, results for MCF10A and MDA-MB-231 cells have been obtained from data adapted from ⁹.

To infer the functions $F(x_i, v_i)$, $f(\Delta x)$, and $\gamma(\Delta x)$ from trajectory data, we use Underdamped Langevin Inference⁵⁴ (Methods). We find that single-cell terms are qualitatively similar across our cell types (Supplementary Fig. 2). By contrast, inferred interactions vary strongly: Breast cancer cells exhibit short-range attraction and pronounced anti-friction⁹ (Fig. 3e,f). The fibrosarcoma cells show repulsive interactions, but exhibit no detectable friction interactions. For the epithelial cell lines, we find repulsion and friction interactions. For all cell lines, the learned equations of motion accurately predict long-time scale behavior statistics (dotted bars in Fig. 3a-c, Supplementary Fig. 5). To summarize these findings with reduced dimensionality⁹, we plot the dominant inferred amplitudes of the cohesion and friction interactions of the various cells (Fig. 3g, Methods). The five different cell lines occupy different regions in this interaction behavior space (IBS) with an apparent correlation between inferred effective cohesion and friction interactions for the various cell types. Together, this inference procedure reveals a variety of different dynamics ranging from attraction and anti-friction of breast cancer cells to repulsion and friction of epithelial cells.

Connecting cell-cell interaction mechanisms to behavior

Next, we ask if the diverse dynamics of pairs of motile cells can be captured by candidate mechanisms in our phenomenological model (Eqs. (1-3)). To construct such mechanisms, we assume only lowest-order linear couplings that behave like vectors in arbitrary dimensions obeying rotational and translational symmetry. As there are 7 different linear vectorial couplings (Fig. 1b) possibly influencing the 3 degrees of freedom in our model through G_n , G_p , and G_r , we consider in total 21 phenomenological cell-cell interaction mechanisms. Further, we impose that interaction mechanisms cannot introduce couplings of the degrees of freedom of the same cell that are not already introduced by the single cell terms (Supplementary Section 4). This reduces the set of interactions to 11 candidates, ranging from couplings of the nuclei and protrusions via repulsion or attraction to various interactions of cell polarity (Fig. 4a). In anticipation of results below, we highlight two mechanisms: polarity-protrusion coupling (PPrC), describing how cells orient their polarity away or towards the protrusion of the other cell, and polarity-polarity coupling (PPC) allowing for alignment or anti-alignment of cell polarity. For all interaction mechanisms, we impose a typical interaction range r and interaction strength ϵ . For instance, for polarity-polarity coupling, we write $G_p = -\epsilon_{PPC} e^{-|\Delta x_p|/r_{PPC}} \Delta P$, where $\Delta P = P_i - P_j$ and $\Delta x_p = x_{p,i} - x_{p,j}$ (Supplementary Section 4.3). Altogether, these interaction mechanisms give rise to various prototypical cell-cell interaction behaviors (Fig. 4a).

To analyze the interaction dynamics emerging from our candidate interaction mechanisms, we numerically simulate cell trajectories (Fig. 4b). First, we infer and analyze the underdamped effective interactions from simulations of each individual candidate interaction. Specifically, varying the amplitude and sign ϵ of each interaction mechanism and employing our inference procedure yields a mapping $f_0(\epsilon)$ and $\gamma_0(\epsilon)$ (Eq. (4)), which we depict in the IBS (Fig. 4c). Intuitively, varying the nucleus coupling strength ϵ_{NC} and thus tuning between nucleus attraction and repulsion corresponds mainly to varying the underdamped cohesion parameter

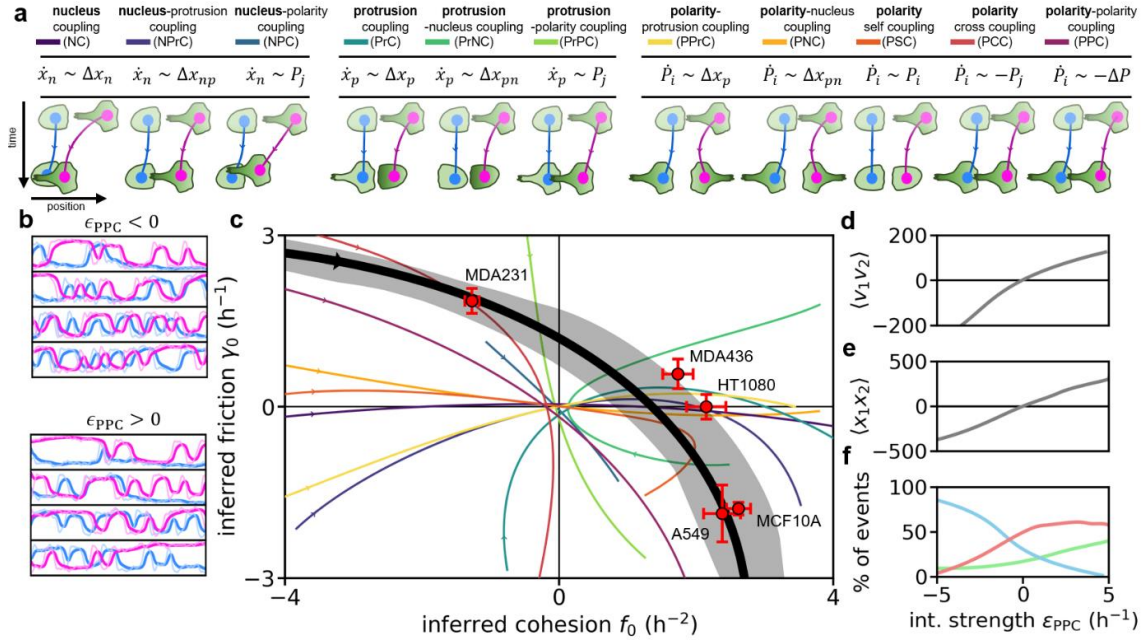


Figure 4 | Underdamped dynamics of cell-cell interaction mechanisms. **a)** Candidate cell-cell interaction mechanisms. The upper row indicates the linear coupling of that mechanisms and the lower row shows a schematic of the expected behavior of cells at the associated interaction strength ϵ being positive. Green color gradient indicates cell polarity. All mechanisms are described in detail in Supplementary Section 4.3 **b)** Nucleus- and protrusion trajectories obtained from simulating the phenomenological model with polarity-polarity coupling interactions for two values of the interaction strength ϵ_{PPC} . **c)** Colored lines show a mapping $(f_0(\epsilon), \gamma_0(\epsilon))$ predicted by the 11 candidate cell-cell interactions while varying the associated interaction strength ϵ . Little arrowheads are located at $\epsilon < 0$ and show the direction in which we increase ϵ . For all curves, $\epsilon \approx 0$ is located at the coordinate center of the IBS. Black curve shows the model prediction of PPC+PPrC that best fits the experimental data of the five different cell lines. Shaded black region around that curve indicates the spread of the model result for 20 best parameter combinations (Methods). Red symbols indicate experimental result. **d)-f)** Behavior statistics predicted by our mechanistic model with the candidate cell-cell interaction PPC. Panel (d) shows the instantaneous velocity correlations, panel (e) shows instantaneous position cross-correlation between the two cells, and panel (f) shows the collision statistics. Curves in panels c-f are slightly smoothed using splines.

f_0 . By contrast, interactions between cell protrusion and polarities give rise to more complicated underdamped dynamics, including friction or anti-friction. Interestingly, only PPC can qualitatively predict the experimentally observed correlations between inferred cohesion and friction interactions when tuning between anti-alignment ($\epsilon_{\text{PPC}} < 0$) and alignment ($\epsilon_{\text{PPC}} > 0$) (violet curve in Fig. 4c). Furthermore, with PPC, we can capture a switch from anti-correlated sliding to correlated reversal behavior when tuning the interaction strength (Fig. 4d,f, Supplementary Fig. 8,9, Supplementary movie 5), as experimentally observed (Fig. 3a,c). These results show that our data-driven inference approach provides strong quantitative constraints on our phenomenological model.

Polarity-polarity coupling tunes between the behavior of various cell types

To quantitatively constrain cell-cell interaction mechanisms, we next perform a fit of our phenomenological model to the experimental data of each cell type. Initially, we take a minimal

approach and allow only a single possible interaction mechanism. To perform the fit, we vary the interaction strength ϵ and range r of the individual mechanisms, and minimize both the difference between the inferred underdamped interactions, as well as between the behavior statistics of model and experiment (Methods). We first consider an individual fit, allowing the interaction mechanism and all parameters to vary between cell types. This fit shows that epithelial and breast cancer cells are best captured by mechanisms like PPC that allow either anti-alignment or alignment between the cells. Fibrosarcoma (HT1080) cells are best described by mechanisms that couple either the polarity or the protrusion to the position of the other cell, reminiscent of CIL (Fig. 5a). In addition, we consider a global fit, where we use the same interaction mechanism for all cell types, allowing only the interaction strength ϵ to vary. Interestingly, the global fit reveals that PPC best captures the dynamics of all cell types, while only varying the coupling strength ϵ_{PPC} between cells (Fig. 5b, Supplementary Fig. 10). However, PPC alone does not quantitatively reproduce the mutual exclusion behavior, the percentage of following events, and the effective repulsion interactions of epithelial and breast cancer cells (Fig. 4c,e,f, Supplementary Fig. 10).

To fully capture the dynamics of epithelial and breast cancer cells, additional interaction mechanisms are required. Indeed, combining PPC with mechanisms that couple the polarity or protrusion to the position of the other cell provides an improved individual and global fit (Fig. 5a,b) to these cells. From these combinations, PPC together with PPrC best captures both the underdamped interactions and the experimental behavior statistics of all cell types (Fig. 5c-f, Supplementary Fig. 14,15, Supplementary movie 6). Here, PPrC with $\epsilon_{\text{PPrC}} > 0$ adds an

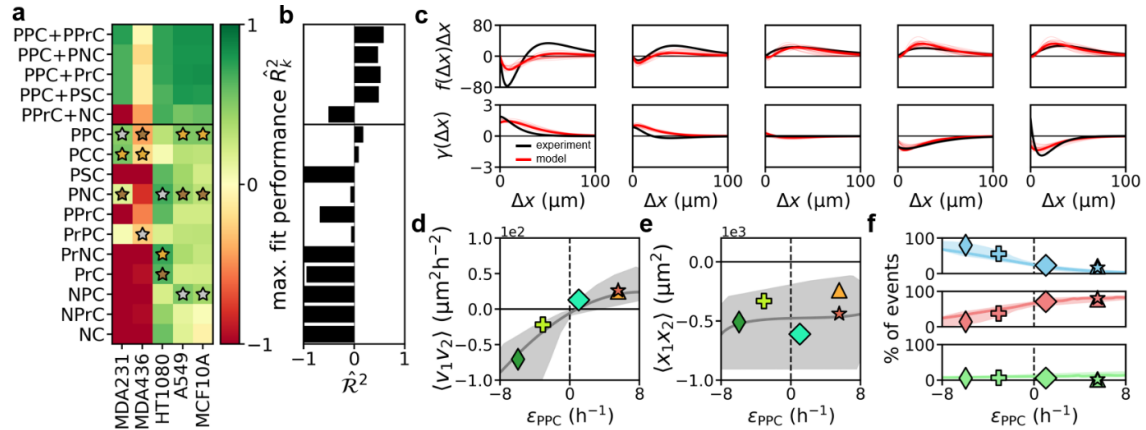


Figure 5 | Quantitative fit of the experimental dynamics. a),b) Maximum fit performance as quantified by the coefficient of determination R^2 for each interaction mechanism using an individual fit (a) and a global fit (b). Here, R^2 is equal to 1 when the model perfectly fits the data and can be negative indicating bad model performance (Methods). Gold, silver and bronze stars indicate the three best fitting interaction mechanisms for each cell type. We show multiple combinations of PPC with mechanisms that well fit the fibrosarcoma HT1080 cells. **c)** Inferred underdamped cohesion and friction interactions for both experiment (black) and model (red) for all the various cell lines. Model result is obtained from the best fitting candidate cell-cell interaction PPC+PPrC. Thin red lines indicate model results for 20 best fitting parameter combinations. **d)-f)** Comparison of behavior statistics between experiment (symbols) and model (curves). Experimental results are plotted at the best fitting coupling strength ϵ_{PPC} for each cell type to facilitate comparison between model and experiment. Panels (d) and (e) show the instantaneous velocity and position correlations respectively. Panel (f) shows percentages of sliding (blue), reversal (red) and following (green) events.

additional repulsive component to the dynamics (Fig. 4c), induces mutual exclusion behavior, and suppresses following behavior (Supplementary Fig. 13). Remarkably, the combined fit of PPC and PPrC is successful even if we allow only the strength of the polarity coupling ϵ_{PPC} to vary between different cell types. We find that the two breast cancer cell lines exhibit anti-alignment with $\epsilon_{\text{PPC}} < 0$. By contrast, the fibrosarcoma cell line exhibits very weak alignment interactions and its dynamics are dominated by PPrC. Finally, the epithelial cells exhibit alignment interactions with $\epsilon_{\text{PPC}} > 0$, yielding correlated velocities and dominant reversal behavior (Supplementary Fig. 11). These results do not depend sensitively on the single cell behavior (Supplementary Fig. 17) or the chosen dumbbell-shaped geometry (Supplementary Fig. 18). Furthermore, considering examples of different pairs of interactions or more than two does not provide a better description of the dynamics of these cell lines (Fig. 5a, Supplementary Fig. 16). Taken together, PPC and PPrC enable cells to adapt their polarity relative to both polarity and position of the other cell, providing a large range of possible behavioral responses to cell-cell collisions. Thus, with these interaction mechanisms we can quantitatively capture a wide variety of interaction behaviors across a broad range of distinct cell types.

Modeling molecular perturbations of cell-cell interaction pathways

We hypothesize that the varying polarity-polarity coupling strength across our cell types originates in different molecular expression profiles of several relevant proteins (Fig. 2b). To test this, we disrupt specific cell-cell interaction pathways through molecular perturbations, which we would then expect to tune the polarity-polarity coupling strength. Specifically, we use antibodies to block E-Cadherin bonds that are established upon contact between two epithelial MCF10A cells (Fig. 6a). These bonds are known to be adhesive and are crucial for collective cell migration of epithelial tissues¹⁸. In addition, we consider perturbations of Eph-ephrin interactions, which directly regulate cell polarity through up- or downregulation of polarity cues such as Cdc42 or RhoA³⁰. Epithelial MCF10A cells express the ligand ephrinA1 (Fig. 6b), which we block using antibodies. Furthermore, we investigate the behavioral shift in MCF10A cells undergoing an epithelial-mesenchymal transition (EMT). This transition changes the coordinated interaction behavior of epithelial cells to that of more individually migrating cells^{17,32,59}. Finally, we induce E-Cadherin in the breast cancer cell line MDA-MB-231 via mRNA transfection (Fig. 6c, Supplementary Section 2.4).

In all these perturbation experiments (Supplementary movie 3,4), we can capture the changing interaction dynamics with our phenomenological model and the combination of polarity-polarity coupling and polarity-protrusion repulsion. Specifically, we observe that blocking of E-Cadherin and Eph-ephrin pathways, as well as EMT in epithelial MCF10A cells reduces the polarity-polarity coupling strength ϵ_{PPC} , thereby inhibiting polarity alignment interactions between MCF10A cells. Consequently, these perturbations reduce positive velocity correlations (Fig. 6d), the number of reversal events observed in MCF10A cells (Fig. 6e), and the amplitudes of the inferred underdamped cohesion and friction interactions (Fig. 6f). Similarly, our model captures the changing dynamics upon transfecting MDA-MB-231 breast cancer cells with E-Cadherin by a reduction of polarity-polarity coupling (Fig. 6f), indicating that E-Cadherin can inhibit anti-alignment interactions in these cells. The E-Cadherin

transfected cells exhibit no significant velocity correlations anymore (Fig. 6g) and fewer sliding events (Fig. 6h). Taken together, our model captures the changing dynamics of cell-cell interactions upon molecular perturbations of the underlying interaction pathways.

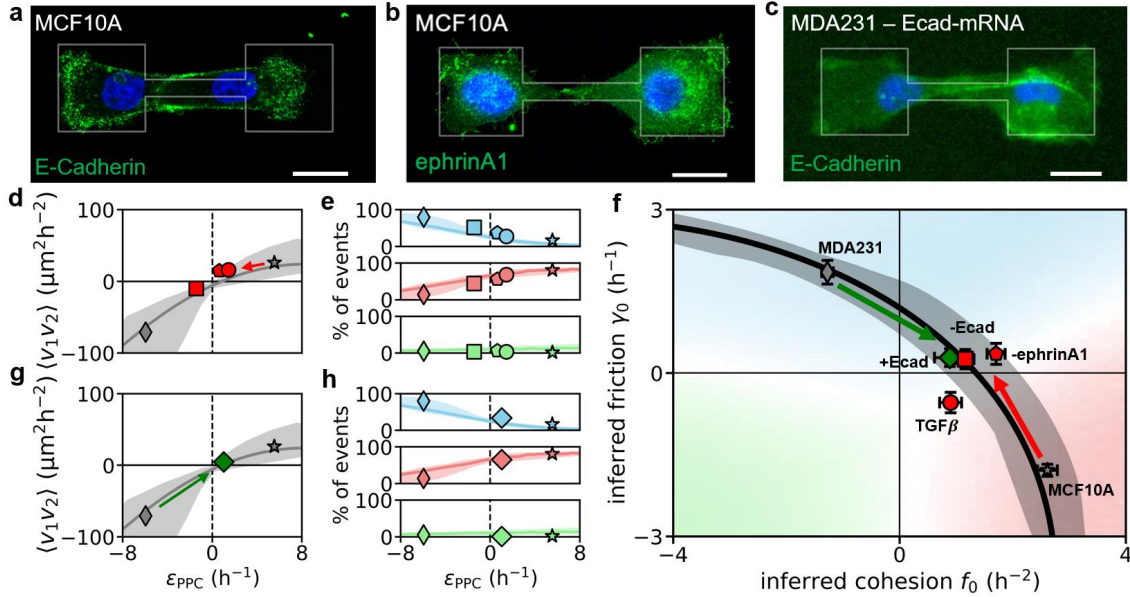


Figure 6 | Capturing molecular perturbations with interaction mechanisms. a),b) Fluorescence images of E-Cadherin expression (a) and ephrinA1 expression (b) in MCF10A cells. c) E-Cadherin expression in transfected MDA-MB-231 cells while confined on the dumbbell-shaped micropattern. Nuclei stained in blue and scale bar for all panels (a)-(c): 20 μm . d) and g) Instantaneous velocity cross-correlation between two cells, when they occupy the same island. Throughout, the solid lines indicates our model result obtained from simulating the phenomenological model with PPC and PPrC varying only ϵ_{PPC} but using the parameters obtained from the global fit to the various cell lines as presented in Fig. 5. Symbols show experimental results of the various perturbed cell lines plotted at the best fitting interaction strength ϵ_{PPC} . e) and h) Percentages of the three different collision events for the five different cell lines. Again, symbols show experimental results and solid line shows model result. f) Interaction behavior space shows the change of the dynamics of the MCF10A and MDA-MB-231 cell lines due to various molecular perturbations. Solid black curve indicates model result from the best global fit of the experimental dynamics of the various cell lines as presented in Fig. 4c.

Discussion

To unravel the mechanisms underlying the interaction behaviors of motile cells, we proposed a phenomenological theory for contact-interactions. Previous work focused on single cell types and either included ad hoc bottom-up models^{6,22,41,47,51,60} or was limited to qualitative analyses of behavior^{38,53}. Here, we proposed 11 unbiased interaction mechanisms which we quantitatively constrain using trajectory data from cell collision experiments with distinct cell types. We find that a combination of only two mechanisms - polarity-polarity coupling (PPC) and polarity-protrusion coupling (PPrC) – is sufficient to describe these cells: Tuning PPC from anti-alignment to alignment of cell polarity quantitatively captures the qualitatively distinct behaviors observed across our cell types. We identify anti-alignment interactions as novel interaction mode, which promotes sliding behavior of breast cancer cells. This interaction is reminiscent of contact enhancement of locomotion²⁴ and may cause doublet-rotations observed for MDCK cells^{38,61}. In contrast, polarity alignment promotes correlated reversal behavior of epithelial cells and may be related to mechanisms of epithelial tissue migration^{41,46,62–64}. PPrC, which causes polarities to grow away from the other cell similar to contact inhibition of locomotion^{10,28}, captures the mutual exclusion behavior of all our cells. Despite the complexity of the cellular interaction machinery, our results reveal that the emergent large-scale behaviors of distinct interacting cells are captured by two simple polarity interaction mechanisms.

To challenge our theory, we performed various molecular perturbations of surface proteins that likely signal to the polarity machinery of cells. By blocking the function of E-Cadherins^{31,59,65} and cell-cell recognition via Eph-ephrin interactions^{16,29}, we demonstrated that these surface proteins set the strength of polarity-polarity coupling. Furthermore, activating expression of E-Cadherin inhibits anti-alignment in cancerous MDA-MB-231 cells, which may be interpreted as a partial reversion of their mesenchymal phenotype⁶⁶. Given our finding that tuning the sign and strength of polarity-polarity coupling captures various cell types, multiple molecular perturbations, and complex processes like the epithelial-mesenchymal transition, polarity-polarity coupling may be a robust and conserved mechanism underlying contact-interactions between cells.

Polarity-polarity coupling has been invoked in toy models for active matter⁶⁷ and captures the tissue-scale flocking behavior of epithelial MDCK cells on 1D tracks^{41,51,64}. Here, we showed in an unbiased way that such polarity interactions accurately capture the collision dynamics of epithelial and breast cancer cells on a two-cell level. As our model readily generalizes to 2D and 3D, polarity-polarity coupling may introduce polar order on the level of two cells within small migrating epithelial cell clusters^{41,43,44,51}, 2D epithelial tissues^{4,62,68,69}, or collective rotations of 3D organoids⁷⁰. In contrast, the loss of polar order is associated with cancer progression and cancer cells exhibit nonaligned disordered motion in 2D sheets^{33,71}. This loss of order may be related to anti-alignment interactions, which could lead to disordered cell spreading⁴² or fluid like disordered collective behavior^{72–74}. Thus, our phenomenological theory could give insight into how contact-interactions at the cellular level control collective cell migration of epithelial and mesenchymal cells.

Methods

Micropatterning and sample preparation

For the cell experiments, we employ a micropattern structure with a dumbbell shaped design with two 35x35 μm squares connected by a 40x7 μm bridge⁹. For micropatterning, we employ a photopatterning technique using the PRIMO module (Alvéole). For background passivation of the μ -dish (ibidi), a drop of 0.01% (w/v) PLL (Sigma-Aldrich) is added and incubated for 30 min. Afterwards, the sample is rinsed with HEPES buffer (Sigma-Aldrich) and 100mg/ml PEG-SVA (LaysanBio) is incubated for 1 h at room temperature. The passivated dish is photopatterned by employing the PRIMO module mounted on an automated inverted microscope (Nikon Ti Eclipse). The photoinitiator PLPP (Alvéole) is added to the dish. The dumbbell shaped pattern was placed on top of the dish via the Leonardo software (Alvéole) and illuminated with UV-light with a dose of 15 mJ/mm². The dish is washed with milliQ water and rehydrated with PBS for 5 min followed by an incubation with 20 $\mu\text{g/ml}$ of labelled Fibronectin-Alexa647 (YO-protein, ThermoFisher) for 15 minutes at room temperature. For antibody blocking experiment fibronectin micropatterns are made by microplasma-initiated protein patterning as described in⁵⁶.

Cell Culture

The cell lines MDA-MB-231, MDA-MB436, HT-1080, A549 and MCF10A were used in this study. The individual culture condition can be found in Supplementary table 1. Cells are grown at 37°C in an atmosphere containing 5% CO₂. For passaging, cells are being washed and treated with accutase for 5 min. The cell solution is centrifuged at 800 r.c.f. for 3 min and the cells are resuspended in medium. Approximately 10 000 cells are added into the micropatterned μ -dish and left to adhere for up to 4h in the incubator. After this incubation period, the medium is exchanged for phenol red free medium and 25nM Hoechst 33342 (Invitrogen) is added to stain the nuclei when needed.

Inhibitors and Antibody blocking

In order to block the function of E-Cadherin or ephrinA1, blocking antibody CD324 (functional grade, Invitrogen) or anti-ephrinA1 antibody (Invitrogen, ThermoFisher) was added to the dish after cells adhered to the pattern at a concentration of 5 $\mu\text{g/ml}$ and 1 $\mu\text{g/ml}$ respectively. After an incubation period of 1h, time-lapse measurements were started. EMT was induced by 10ng/ml treatment with TGF β (ThermoFisher) for up to 7 days.

Transfection

Prior to the transfection, cells were seeded in an μ -dish (ibidi) without patterning. At 90% confluency the cells were transfected with LipofectamineTM 2000 (Invitrogen, Germany) complexes containing E-Cadherin mRNA (Supplementary Section 2.4). First, 2 μl LipofectamineTM 2000 reagent are mixed with 398 μl OptiMEM (Invitrogen, Germany) and incubated for 5 min at room temperature. Simultaneously, 2 μl mRNA (1735 ng/ μl) is diluted in 198 μl OptiMEM. The mRNA mix is added onto 200 μl of the LipofectamineTM 2000 dilution and incubated for 20min at room temperature. Cells are washed once with OptiMEM and then the lipoplexes are added to the dish. After 1h, cells are washed again and re-incubated with normal medium. For control experiments, lipoplexes were created with either GFP-mRNA or substituted with milliQ water at the same ratio. For more details see Supplementary Section 2.4.

Microscopy and Cell Tracking

All measurements are performed in time-lapse mode for 48 h on a Nikon Eclipse Ti microscope or on a Nikon Eclipse Ti2 microscope using a 10× objective. The samples are kept in a heated chamber (Okolab) at 37 °C at 5% CO2 throughout the measurements. Every 10 min a bright-field image and a fluorescence image of the stained nuclei are acquired. Cell tracking of the Nuclei is performed by using TrackPy. Track length varied between 8 h and 48h. For more details see Supplementary Section 2.2 and 2.3.

Western Blots

Cells were harvested and lysed in RIPA lysis buffer supplemented with 1M PMSF and a protease inhibitor cocktail (ThermoFisher). Lysates were centrifuged at 14 000g for 20min at 4°C. Supernatant was transferred and stored at -80°C. Protein concentration were determined by Bradford assay and an equal amount of protein was loaded onto the precast SDS-gel (BioRad). Proteins were separated by gel electrophoresis. The transfer was performed on Immuno-Blot polyvinylidene difluoride (PVDF) membranes (BioRad) with the Transblot turbo transfer system (BioRad) during 7 min. After blocking for 1h with 5% non-fat dried milk (ThermoFisher) in PBS 0.1% Tween 20 (Roth) the membranes were probed with primary antibodies mouse anti-ECAD (ThermoFisher) (1:1000) and rabbit anti-NCAD (ThermoFisher) (1:2000) overnight at 4°C. Secondary antibodies HRP-anti-mouse IgG (1:10000) and HRP-anti-rabbit IgG (1:10000) were incubated on the membrane for 1h at room temperature. Development was performed using Pierce western ECL substrate (ThermoFisher) and the ChemiDoc Imaging System (BioRad). The intensity of the band was quantified via densitometry using ImageJ and protein amount was normalized to a β -actin loading control on the same membrane.

Immunohistochemistry

The cells were fixed after the experiment with 4% PFA for 10min. Cells were washed three times with PBS. Afterwards the cells were permeabilized for 5 min in 0.1% Triton-X-100 solution (Sigma) and blocked for 1h in cold 4% BSA (ThermoFisher). The cells were rinsed once with cold 1% BSA. The excess liquid was removed and the cells were subjected to primary antibodies mouse anti-ECAD (ThermoFisher) (1:100) and rabbit anti-ephrinA1 (ThermoFisher) (1:100) diluted in 1% BSA overnight at 4°C. Three washes with 1% BSA were carried out before the adding of the secondary antibody AlexaFluor 488 goat anti-mouse (ThermoFisher) (1:1000) or Alexa 647 goat anti-rabbit (ThermoFisher) (1:1000) for 1h in the dark. The solution was then removed and washed 3 times with PBS. F-Actin staining was done with rhodamine-phalloidin (ThermoFisher, 1:1000). Cells were imaged on a Confocal LSM980 microscope using the airy scan mode with a 40x water immersion objective.

Model development

Based on previous work^{39,40,49,75,76}, we employ a generalized active particle model to describe pairs of interacting cells. To this end, we generalize a previously employed mechanistic model for single migrating cells in confinement³⁴:

$$\begin{aligned}\dot{x}_{n,i} &= -\frac{k_n}{\gamma(x_{n,i})}(x_{n,i} - x_{p,i}) + G_n(\Delta x, P, \Delta P) \\ \dot{x}_{p,i} &= k_p(x_{n,i} - x_{p,i}) + P_i(t) + G_p(\Delta x, P, \Delta P) + F_{\text{boundary}}(x_{p,i}) \\ \dot{P}_i &= -\alpha(x_{p,i})P_i - \beta P_i^3 + G_p(\Delta x, P, \Delta P) + \sigma \eta_i(t).\end{aligned}$$

Here, the nucleus and the protrusion of the same cell are coupled by a linear spring and $k_n = k/\zeta_n$ and $k_p = k/\zeta_p$ are the spring constants reduced by the friction coefficients of the cell nucleus ζ_n and the cell protrusion ζ_p , respectively. Furthermore, $\gamma(x_{n,i})$ is a dimensionless rescaling factor of the friction coefficient ζ_n that depends on the position of the cell nucleus with a minimum when the cell nucleus is on the bridge. This models the reduced adhesive area accessible to the cell on the bridge, which is a key feature of confined cell migration on our dumbbell-shaped micropattern³⁴. The cell's protrusion is confined on the micropattern by a boundary force $F_{\text{boundary}}(x_{p,i})$, which represents a soft repulsive force at the boundaries of the micropattern. In this model, the polarity of the cell is guided by the geometry of the micropattern^{34,35}. Specifically, the polarity switches from a negative feedback loop on the island to a positive feedback loop on the bridge of the micropattern, causing the polarity to grow into the bridge as cells transition between the islands. This is implemented by the function $\alpha(x_{p,i})$, which becomes negative when the protrusion $x_{p,i}$ is on the bridge. The higher order term $-\beta P_i^3$ prevents unbound growth of the polarity and gives rise to a preferred polarity when $\alpha(x_{p,i})$ is negative. The interaction terms G_n , G_p , and G_P encode phenomenological interaction mechanisms, which we derive in an unbiased way. The term $\sigma\eta_i(t)$ encodes uncorrelated Gaussian white noise, modeling the inherent stochasticity of cell polarity and cell migration. For more details refer to Supplementary Section 4.1-4.3.

Behavior statistics

To quantify interaction behavior of pairs of motile cells, we compute several behavior statistics introduced in the literature⁹. First, we find the correlation functions $C_V(|t - t'|) = \langle v_1(t)v_2(t') \rangle_{\text{same}}$ and $C_X(|t - t'|) = \langle x_1(t)x_2(t') \rangle$. For both these correlation functions, we define $t' = t + \Delta$ and then average the products of the velocities or positions of the two cells over time t and all pairs of cells. For C_V , we condition our averaging on both cells being located on the same island. For easy visualization, we show in the main text figures the instantaneous correlations ($|t - t'| = 0$) and show the full result in Supplementary Fig. 5. Furthermore, we detect collision events in our cell trajectories by defining a threshold $\Delta x < \Delta x_c$, where Δx is the intercellular distance. Then we analyze the trajectories within a time frame of dT following the first time when $\Delta x < \Delta x_c$. If cells simultaneously transition from one island to the other, we detect a following event. If cells switch positions at least once during dT , we detect a sliding event. Finally, if cells do not switch positions during dT , we detect a reversal event. The collision statistics is robust against the choice of parameters of the detection algorithm.

Data-driven inference

We perform a data-driven inference approach to learn effective dynamical interaction terms that govern the short time scale dynamics of the nuclei of interacting cells^{9,52,54}. This approach involves proposing coupled underdamped Langevin equations for the nucleus trajectories $x(t)$ of the two cells⁹ (Eq. 4). The key idea of this approach is to estimate from the experimentally measured nucleus trajectory $x(t)$ both the instantaneous velocity $\hat{v}(t)$ and the instantaneous acceleration $\hat{a}(t)$, while considering errors introduced by the discrete sampling and possible measurement errors. Then, assuming that the Langevin equation can capture the dynamics of these cells, we can rigorously infer the deterministic single cell term $F(x_i, v_i)$ and the interaction terms $f(\Delta x)\Delta x$ and $\gamma(\Delta x)\Delta v$ on the right hand side of equation 4 using stochastic estimators⁵⁴. Briefly, this is done by fitting the experimental accelerations, measured over the phase space of our system, by the deterministic terms expanded in sets of basis functions. Throughout, we expand the interaction terms into exponentials of the form $b_n(|\Delta x|) = e^{-|\Delta x|/nr}$, where $n = 1, \dots, N$. Thus, for instance $f(\Delta x) \approx \sum_n u_n b_n(|\Delta x|)$ and the coefficients u_n get estimated rigorously from the trajectory data⁵⁴. This procedure is robust against the

choice of basis function⁹, but the experimental data is best captured at certain values of N . For MCF10A, MDA231, and MDA436 cells, we use $N = 3$ and $r = 20 \mu m$. For A549 cells we use $N = 2$ and $r = 25 \mu m$ and for HT1080 cells, we use $N = 1$ and $r = 30 \mu m$. Note that for HT1080 cells, we found that the best Langevin equation is one without the term $\gamma(\Delta x)\Delta v$. Finally, to predict the interaction behavior space (IBS), we fix $N = 1$ and $r = 30 \mu m$ and vary manually u_n which we defined as either f_0 or γ_0 . For each parameter combination, we simulate trajectories and find the dominant collision behavior, which we depict as colormap in Fig. 3g. For the position of the experimental cell lines, we perform the inference procedure with $N = 1$ and $r = 30 \mu m$ giving f_0 or γ_0 .

Fitting procedure

To fit our phenomenological model to the experimental data, we sweep over the interaction strength ϵ and interaction range r of each candidate interaction mechanisms as well as for each pair of mechanisms. For each parameter combination, we predict the velocity cross correlation $C_V(|t - t'|)$, the position cross correlation $C_X(|t - t'|)$, and find the collision distribution. Note that in the fitting procedure, we only consider $|t - t'| < \tau$ to avoid fitting the correlations that are close to zero in the experiment. For C_V we choose $\tau = 0.5 h$ and for C_X we choose $\tau = 10 h$. Furthermore, we perform our data-driven inference method to find the underdamped cohesion $f(\Delta x)\Delta x$ and friction interactions $\gamma(\Delta x)\Delta v$ from the simulated data. For each of these five statistics, we compute the so called Coefficient of determination (COD) defined by $R^2 = 1 - SS_{\text{res}}/SS_{\text{tot}}$, where SS_{res} is the sum of squared deviations between model and experiment: $SS_{\text{res}} = \sum_i (y_i - \hat{y}_i)^2$ with y_i being the experimental result and \hat{y}_i being the model result for the five different statistics. The index i runs over the discrete values of the numerically computed statistics. $SS_{\text{tot}} = \sum_i (y_i - \bar{y}_i)^2$ is related to the variance of the experimental data. Consequently, R^2 is equal to 1 if the model perfectly captures the experimental data but equal to 0 if the model merely captures the mean of the experimental data. R^2 is negative when the model performs even worse than that. To perform a simultaneous fit to all five statistics, we average R^2 over all statistics. For the individual fit, we then maximize the resulting average $R^2(\epsilon, r)$ for each cell type individually. This gives us optimal parameters $\hat{\epsilon}$ and \hat{r} for each cell type. For the global fit, we first fix the interaction strength r and then maximize the averaged R^2 for each cell by varying the interaction strength ϵ . Then we again average R^2 across cell types for each interaction strength r . After that, we maximize R^2 averaged over all statistics and cell types, giving us a single optimal value \hat{r} , but varying interaction strengths for each cell type $\hat{\epsilon}$. Throughout, we adjust the bounds of the parameters ϵ and r such that we at least include a local maximum of $R^2(\epsilon, r)$. For more details refer to Supplementary Section 4.5.

Statistical analysis

Throughout, error bars indicate the standard error of the mean (s.e.m) which we obtain for experimental data by bootstrapping. Specifically, we draw random subsets of the trajectory data, compute the quantity of interest, and then average the standard deviations over the different subsets. For the error bars of the statistics predicted by the inferred Langevin equation as presented by dotted bars in Fig. 4a-c, we again bootstrap the experimental data, perform the inference procedure and re-simulate the inferred equation to predict these statistics. The error bars then again represent the error of the mean across these bootstrapped subsets of the data. For the phenomenological model, we indicate the variability of the predicted behavior statistics and inferred underdamped interaction terms by showing the spread of the 20 best fitting parameter combinations. For model results, we typically simulate $N = 300$ trajectories. The number of experimental trajectories is given in Supplementary table 1.

Data availability

Experimental and simulation data is available from the corresponding author upon request.

Code availability

Python code to analyze data and perform numerical simulations is available from the corresponding author upon request.

References

1. Haeger, A., Wolf, K., Zegers, M. M. & Friedl, P. Collective cell migration: Guidance principles and hierarchies. *Trends Cell Biol.* **25**, 556–566 (2015).
2. Mishra, A. K., Campanale, J. P., Mondo, J. A. & Montell, D. J. Cell interactions in collective cell migration. *Development* **146**, 1–7 (2019).
3. Scarpa, E. & Mayor, R. Collective cell migration in development. *J. Cell Biol.* **212**, 143–155 (2016).
4. Poujade, M. *et al.* Collective migration of an epithelial monolayer in response to a model wound. *Proc. Natl. Acad. Sci. U. S. A.* **104**, 15988–15993 (2007).
5. Friedl, P. & Wolf, K. Tumour-cell invasion and migration: diversity and escape mechanisms. *Nat. Rev. Cancer* **3**, 362–374 (2003).
6. Vedel, S. *et al.* Migration of cells in a social context. *Proc. Natl. Acad. Sci. U. S. A.* **110**, 129–134 (2013).
7. Abercrombie, M. Contact inhibition and malignancy. *Nature* **281**, 259–262 (1979).
8. Scarpa, E. *et al.* A novel method to study contact inhibition of locomotion using micropatterned substrates. *Biol. Open* **5**, 1553 (2016).
9. Brückner, D. B. *et al.* Learning the dynamics of cell–cell interactions in confined cell migration. *Proc. Natl. Acad. Sci. U. S. A.* **118**, (2021).
10. Roycroft, A. & Mayor, R. Molecular basis of contact inhibition of locomotion. *Cell. Mol. Life Sci.* **73**, 1119–1130 (2016).
11. Collins, C. & Nelson, W. J. Running with neighbors: Coordinating cell migration and cell-cell adhesion. *Curr. Opin. Cell Biol.* **36**, 62–70 (2015).
12. Ladoux, B. & Mège, R. M. Mechanobiology of collective cell behaviours. *Nat. Rev. Mol. Cell Biol.* **18**, 743–757 (2017).
13. Ridley, A. J. Life at the leading edge. *Cell* **145**, 1012–1022 (2011).
14. Rappel, W. J. & Edelstein-Keshet, L. Mechanisms of cell polarization. *Curr. Opin. Syst. Biol.* **3**, 43–53 (2017).
15. Danuser, G., Allard, J. & Mogilner, A. Mathematical modeling of eukaryotic cell migration: Insights beyond experiments. *Annu. Rev. Cell Dev. Biol.* **29**, 501–528 (2013).
16. Kadir, S. *et al.* Microtubule remodelling is required for the front-rear polarity switch during contact inhibition of locomotion. *J. Cell Sci.* **124**, 2642–2653 (2011).
17. Theveneau, E. & Mayor, R. Collective cell migration of epithelial and mesenchymal cells. *Cell. Mol. Life Sci.* **70**, 3481–3492 (2013).
18. Jain, S. *et al.* The role of single-cell mechanical behaviour and polarity in driving collective cell migration. *Nat. Phys.* **16**, 802–809 (2020).
19. Carmona-Fontaine, C. *et al.* Contact inhibition of locomotion in vivo controls neural crest directional migration. *Nature* **456**, 957–961 (2008).
20. Theveneau, E. *et al.* Collective Chemotaxis Requires Contact-Dependent Cell Polarity. *Dev. Cell* **19**, 39–53 (2010).
21. Davis, J. R. *et al.* Emergence of embryonic pattern through contact inhibition of

- locomotion. *Development* **139**, 4555–4560 (2012).
22. Villar-Cervino, V. *et al.* Contact Repulsion Controls the Dispersion and Final Distribution of Cajal-Retzius Cells. *Neuron* **77**, 457–471 (2013).
 23. Mayor, R. & Carmona-Fontaine, C. Keeping in touch with contact inhibition of locomotion. *Trends Cell Biol.* **20**, 319–328 (2010).
 24. D’alessandro, J. *et al.* Contact enhancement of locomotion in spreading cell colonies. *Nat. Phys.* **13**, 999–1005 (2017).
 25. Hayakawa, M. *et al.* Polar pattern formation induced by contact following locomotion in a multicellular system. *Elife* **9**, 1–18 (2020).
 26. Mendonsa, A. M., Na, T. Y. & Gumbiner, B. M. E-cadherin in contact inhibition and cancer. *Oncogene* **37**, 4769–4780 (2018).
 27. Maître, J. L. & Heisenberg, C. P. Three functions of cadherins in cell adhesion. *Curr. Biol.* **23**, 626–633 (2013).
 28. Stramer, B. & Mayor, R. Mechanisms and in vivo functions of contact inhibition of locomotion. *Nat. Rev. Mol. Cell Biol.* **18**, 43–55 (2017).
 29. Astin, J. W. *et al.* Competition amongst Eph receptors regulates contact inhibition of locomotion and invasiveness in prostate cancer cells. *Nat. Cell Biol.* **12**, (2010).
 30. Noren, N. K. & Pasquale, E. B. Eph receptor-ephrin bidirectional signals that target Ras and Rho proteins. *Cell. Signal.* **16**, 655–666 (2004).
 31. Desai, R. A. *et al.* Cell polarity triggered by cell-cell adhesion via E-cadherin. *J. Cell Sci.* **122**, 905–911 (2009).
 32. Scarpa, E. *et al.* Cadherin Switch during EMT in Neural Crest Cells Leads to Contact Inhibition of Locomotion via Repolarization of Forces. *Dev. Cell* **34**, 421–434 (2015).
 33. Wong, I. Y. *et al.* Collective and individual migration following the epithelial–mesenchymal transition. *Nat. Mater.* **13**, (2014).
 34. Brückner, D. B. *et al.* Geometry Adaptation of Protrusion and Polarity Dynamics in Confined Cell Migration. *Phys. Rev. X* **12**, 31041 (2022).
 35. Flommersfeld, J. *et al.* Geometry-Sensitive Protrusion Growth Directs Confined Cell Migration. *Phys. Rev. Lett.* **132**, 98401 (2024).
 36. Edelstein-Keshet, L., Holmes, W. R., Zajac, M. & Dutot, M. From simple to detailed models for cell polarization. *Philos. Trans. R. Soc. B Biol. Sci.* **368**, (2013).
 37. Sens, P. Stick-slip model for actin-driven cell protrusions, cell polarization, and crawling. *Proc. Natl. Acad. Sci. U. S. A.* **117**, 24670–24678 (2020).
 38. Camley, B. A. *et al.* Polarity mechanisms such as contact inhibition of locomotion regulate persistent rotational motion of mammalian cells on micropatterns. *Proc. Natl. Acad. Sci. U. S. A.* **111**, 14770–14775 (2014).
 39. Smeets, B. *et al.* Emergent structures and dynamics of cell colonies by contact inhibition of locomotion. *Proc. Natl. Acad. Sci. U. S. A.* **113**, 14621–14626 (2016).
 40. Sepúlveda, N. *et al.* Collective Cell Motion in an Epithelial Sheet Can Be Quantitatively Described by a Stochastic Interacting Particle Model. *PLoS Comput. Biol.* **9**, 1–12 (2013).
 41. Ron, J. E. *et al.* Polarization and motility of one-dimensional multi-cellular trains. *Biophys. J.* **122**, 4598–4613 (2023).
 42. D’alessandro, J. *et al.* Contact enhancement of locomotion in spreading cell colonies. *Nat. Phys.* **13**, 999–1005 (2017).
 43. Copenhagen, K. *et al.* Frustration-induced phases in migrating cell clusters. *Sci. Adv.* **4**, eaar8483 (2018).
 44. Vercruyssen, E. *et al.* Geometry-driven migration efficiency of autonomous epithelial cell clusters. *Nat. Phys.* (2024) doi:10.1038/s41567-024-02532-x.
 45. Kulawiak, D. A., Camley, B. A. & Rappel, W. J. Modeling Contact Inhibition of

- Locomotion of Colliding Cells Migrating on Micropatterned Substrates. *PLoS Comput. Biol.* **12**, (2016).
46. Jain, S. *et al.* The role of single-cell mechanical behaviour and polarity in driving collective cell migration. *Nat. Phys.* **16**, 802–809 (2020).
 47. Desai, R. A., Gopal, S. B., Chen, S. & Chen, C. S. Contact inhibition of locomotion probabilities drive solitary versus collective cell migration. *J. R. Soc. Interface* **10**, (2013).
 48. Zisis, T. *et al.* Disentangling cadherin-mediated cell-cell interactions in collective cancer cell migration. *Biophys. J.* **121**, 44–60 (2022).
 49. Alert, R. & Trepat, X. Physical Models of Collective Cell Migration. *Annu. Rev. Condens. Matter Phys.* **11**, 77–101 (2020).
 50. Löber, J., Ziebert, F. & Aranson, I. S. Collisions of deformable cells lead to collective migration. *Sci. Rep.* **5**, 1–7 (2015).
 51. Bertrand, T. *et al.* Clustering and ordering in cell assemblies with generic asymmetric aligning interactions. *Phys. Rev. Res.* **6**, 34–38 (2024).
 52. Brückner, D. B. & Broedersz, C. P. Learning dynamical models of single and collective cell migration: a review. 1–62 (2023).
 53. Scarpa, E. *et al.* A novel method to study contact inhibition of locomotion using micropatterned substrates. *Biol. Open* **2**, 901–906 (2013).
 54. Brückner, D. B., Ronceray, P. & Broedersz, C. P. Inferring the Dynamics of Underdamped Stochastic Systems. *Phys. Rev. Lett.* **125**, (2020).
 55. Agliari, E. *et al.* A statistical inference approach to reconstruct intercellular interactions in cell migration experiments. *Sci. Adv.* **6**, 1–11 (2020).
 56. Brückner, D. B. *et al.* Stochastic nonlinear dynamics of confined cell migration in two-state systems. *Nat. Phys.* **15**, 595–601 (2019).
 57. Pollard, T. D. The cytoskeleton, cellular motility and the reductionist agenda. *Nature* **422**, 741–745 (2003).
 58. Blick, T. *et al.* Epithelial mesenchymal transition traits in human breast cancer cell lines. *Clin. Exp. Metastasis* **25**, 629–642 (2008).
 59. Milano, D. F., Ngai, N. A., Muthuswamy, S. K. & Asthagiri, A. R. Regulators of Metastasis Modulate the Migratory Response to Cell Contact under Spatial Confinement. *Biophys. J.* **110**, 1886–1895 (2016).
 60. Zadeh, P. & Camley, B. A. Picking winners in cell-cell collisions: Wetting, speed, and contact. *Phys. Rev. E* **106**, 1–21 (2022).
 61. Lu, L. *et al.* Polarity-driven three-dimensional spontaneous rotation of a cell doublet. *bioRxiv* (2022).
 62. Serra-Picamal, X. *et al.* Mechanical waves during tissue expansion. *Nat. Phys.* **8**, 628–634 (2012).
 63. Tambe, D. T. *et al.* Collective cell guidance by cooperative intercellular forces. *Nat. Mater.* **10**, 469–475 (2011).
 64. Lo Vecchio, S. *et al.* Spontaneous rotations in epithelia as an interplay between cell polarity and boundaries. *Nat. Phys.* **20**, 322–331 (2024).
 65. Nakagawa, M. *et al.* Recruitment and activation of Rac1 by the formation of E-cadherin-mediated cell-cell adhesion sites. *J. Cell Sci.* **114**, 1829–1838 (2001).
 66. Chao, Y. L., Shepard, C. R. & Wells, A. Breast carcinoma cells re-express E-cadherin during mesenchymal to epithelial reverting transition. *Mol. Cancer* **9**, 1–18 (2010).
 67. Vicsek, T. Novel Type of Phase Transition in a System of Self-Driven Particles. *Phys. Rev. Lett.* **75**, 1226–1229 (1995).
 68. Streichan, S. J. *et al.* Global morphogenetic flow is accurately predicted by the spatial distribution of myosin motors. *Elife* **7**, e27454 (2018).

69. Peyret, G. *et al.* Sustained Oscillations of Epithelial Cell Sheets. *Biophys. J.* **117**, 464–478 (2019).
70. Brandstätter, T. *et al.* Curvature induces active velocity waves in rotating multicellular spheroids. *Nat. Commun.* **14**, 1–11 (2021).
71. Lee, R. M., Vitolo, M. I., Losert, W. & Martin, S. S. Distinct roles of tumor associated mutations in collective cell migration. *Sci. Rep.* **11**, 1–12 (2021).
72. Malinverno, C. *et al.* Endocytic reawakening of motility in jammed epithelia. *Nat. Mater.* **16**, 587–596 (2017).
73. Kang, W. *et al.* A novel jamming phase diagram links tumor invasion to non-equilibrium phase separation. *iScience* **24**, (2021).
74. Palamidessi, A. *et al.* Unjamming overcomes kinetic and proliferation arrest in terminally differentiated cells and promotes collective motility of carcinoma. *Nat. Mater.* **18**, 1252–1263 (2019).
75. Szabó, A. & Mayor, R. Modelling collective cell migration of neural crest. *Current Opinion in Cell Biology* vol. 42 22–28 (2016).
76. Belmonte, J. M. *et al.* Self-propelled particle model for cell-sorting phenomena. *Phys. Rev. Lett.* **100**, 248702 (2008).

Acknowledgements:

We thank Johannes Flommersfeld, Bram Hoogland, and Ricard Alert for helpful discussions. We thank Gerlinde Schwake for producing the E-Cadherin mRNA. Funded by the Deutsche Forschungsgemeinschaft (DFG, German Research Foundation) - Project-ID 201269156 - SFB 1032 (Project B01 and B12).

Author Contributions:

E.B. and J.R. designed experiments; E.B. and G.L. performed experiments; T.B., D.B.B., and E.B. analyzed data; T.B. developed model and performed simulations; T.B., E.B., D.B.B., J.R. and C.P.B. interpreted the results and wrote the manuscript. J.R. and C.P.B. conceived this study and led the research. All authors edited and approved the manuscript.

Competing interests:

The authors declare no competing interests.

Supplementary Information:

Learning a phenomenological theory for contact-interactions between motile cells from collision experiments

Tom Brandstätter*, Emily Brieger*, David B. Brückner, Georg Ladurner, Joachim Rädler, Chase P. Broedersz[†]

* These authors contributed equally to this work: Tom Brandstätter, Emily Brieger

[†] Corresponding author: c.p.broedersz@vu.nl, Phone: +31 20 59 82953

Contents

1	Supplementary movie captions	23
2	Supplementary experimental details	24
2.1	Cell culture conditions	24
2.2	Cell exclusion criteria	24
2.3	Tracking procedure and resulting cell trajectories	24
2.4	Experimental details of perturbations	26
2.4.1	EMT in MCF10A cells	26
2.4.2	mRNA construction	26
3	Supplementary analysis of the experimental data	28
3.1	Single cell behavior of the different cell types	28
3.1.1	Dynamics of single cell behavior of cell types	28
3.1.2	Robustness of the single cell behavior	29
3.1.3	Single cell behavior after perturbations	30
3.2	Controlling E-Cadherin transfection	31
3.3	Complete quantification of the experimental nucleus dynamics	31
4	Model development and fitting procedure	33
4.1	Model definition	33
4.2	Overview of model strategy	34
4.3	Complete description of cell-cell interaction mechanisms	35
4.4	Model implementation	37
4.5	Model fitting	38
4.5.1	The coefficient of determination	38
4.5.2	Individual fit of the dynamics	38
4.5.3	Global fit of the dynamics	39
5	Supplementary model results	41
5.1	Comparing the dynamics of candidate cell-cell interactions	41
5.1.1	Underdamped dynamics of candidate cell-cell interactions	41
5.1.2	Summary of qualitative comparison of candidate cell-cell interactions	44
5.2	Quantitative fitting of the dynamics with PPC	47
5.3	Interaction behavior arising from PPC	48
5.3.1	Polarity alignment enables reversal behavior	48
5.3.2	Polarity anti-alignment promotes sliding behavior	49
5.4	Constraining power of inferred interactions	49
5.5	Combining candidate cell-cell interactions	50
5.5.1	Underdamped dynamics of combined interactions	51
5.5.2	Other combinations without PPC	52
5.5.3	More than two interaction mechanisms	53
5.6	The role of single cell behavior	55
5.7	Polarity-polarity coupling on rectangular patterns	57

1 Supplementary movie captions

Supplementary movie 1: Bright field movies of various different migrating pairs of cells on a dumbbell-shaped micropattern. The nuclei of the cells are stained in blue. The dumbbell-shaped micropattern is stained in red. Scale bar is equal to $30\ \mu\text{m}$. Time code is in units of hours (h).

Supplementary movie 2: Bright field movies of various single migrating cells on a dumbbell-shaped micropattern. The nuclei of the cells are stained in blue. The dumbbell-shaped micropattern is stained in red. Scale bar is equal to $30\ \mu\text{m}$. Time code is in units of hours (h).

Supplementary movie 3: Bright field movies of epithelial MCF10A cells with various different biomolecular perturbations on a dumbbell-shaped micropattern. Upper left shows the wildtype, upper right shows the cells with ephrinA1 antibodies, lower left shows MCF10A cells with TGF β -induced epithelial-mesenchymal transition, and lower right shows MCF10A cells with E-Cadherin antibodies. The nuclei of the cells are stained in blue. The dumbbell-shaped micropattern is stained in red. Scale bar is equal to $30\ \mu\text{m}$. Time code is in units of hours (h).

Supplementary movie 4: Bright field movies of breast cancer MDA-MB-231 cells with two different mRNA transfections. Left shows the wildtype, upper right shows the MDA-MB-231 cells with the E-Cadherin transfection, and lower right shows MDA-MB-231 cells with the GFP transfection for control. The nuclei of the cells are stained in blue, and E-Cadherin is stained in green. The dumbbell-shaped micropattern is stained in red. Scale bar is equal to $30\ \mu\text{m}$. Time code is in units of hours (h).

Supplementary movie 5: Animation of the phenomenological model with polarity-polarity coupling for two values of the coupling strength ϵ_{PPC} . Left shows polarity anti-alignment ($\epsilon_{\text{PPC}} < 0$), right shows polarity alignment ($\epsilon_{\text{PPC}} > 0$). Circles indicate the nuclei of the cells and triangles indicate the protrusions of the cells. The grey bar indicates the mechanical coupling of these two degrees of freedom.

Supplementary movie 6: Animation of the phenomenological model with polarity-polarity coupling (PPC) and polarity-protrusion coupling (PPrC) for the five best fitting parameter combinations for the five different cell types as shown in Fig. S15. Circles indicate the nuclei of the cells and triangles indicate the protrusions of the cells. The grey bar indicates the mechanical coupling of these two degrees of freedom.

2 Supplementary experimental details

2.1 Cell culture conditions

For the five cell lines utilized in the experiments, different culture condition and different types of media are used. The exact culture conditions and medium supplements needed for the five different cell lines are listed in Table 1.

Cell line	Medium	Origin
MDAMB231 H2B mCherry	L15 (Gibco) + 10% FBS (Gibco)	Gift from Betz Lab
MDAMB436	L15 (Gibco) + 10% FBS (Gibco)	ATCC
HT1080	MEM (Gibco) + 10% FBS (Gibco) + 5% CO ₂	Authenticated by CLS
A549	RPMI (Gibco)+ 10% FBS (Gibco) 5% CO ₂	DSMZ
MCF10A	DMEM/F-12 (Gibco) + 5% horse serum(Gibco), 20 ng/ml human epidermal growth factor (Sigma), 100 ng/ml cholera toxin (Sigma), 10 μ g/ml insulin (Sigma) and 500ng/ml hydrocortisone (Sigma) + 5% CO ₂	ATCC

Table 1: Cell culture conditions of the different cell lines and their origin.

2.2 Cell exclusion criteria

For each cell line we track the nuclei of a large number of cell pairs confined to the dumbbell shaped micropattern. Following previous work [1], we apply the following criteria for cells to be eligible for tracking:

1. Two-cell trajectories are obtained by either selecting a cell that undergoes division during the duration of the experiment, or by selecting an already attached cell pair at the beginning of the experiment. Tracking is terminated when one of the two cells rounds up for division.
2. The tracks have to be at least 50 consecutive frames (500 min) long.
3. The whole cell including its protrusion has to be confined inside the micropattern.
4. The cells have to be healthy. Abnormalities such as multiple nuclei, disrupted nuclei and occurrences like cell death or detachment from the substrates leads to exclusion of the tracks.

2.3 Tracking procedure and resulting cell trajectories

During the time-lapse measurement (48h), every 10 min a brightfield image and a fluorescence image of the stained nuclei are acquired. Since the micropattern is not visible in the brightfield, one fluorescence

image of the stained dumbbells for each position is taken before the start of the time-lapse measurement. The cell trajectories are determined by using TrackPy (Python Version 3.10.5). After application, the trajectories are inspected manually to correct for tracking mistakes. In the cases where the position of the two cells are mixed up, this is corrected manually. The fluorescence image of the micropattern is used to determine the boundaries of the micropattern and to determine the coordinate origin, which is set at the center of the bridge. The resulting trajectory data sets are summarized in table 2 for all two-cell experiments and in table 3 for all single cell experiments.

cell line	perturbation	micropattern	N	comment
MCF10A	wildtype	dumbbell	251	we perform new experiments and include data adapted from [1]
MCF10A	wildtype	rectangular	96	
MCF10A	E-Cadherin blocking	dumbbell	89	
MCF10A	EphrinA1	dumbbell	103	
MCF10A	TGF β	dumbbell	101	
A549	wildtype	dumbbell	100	
HT1080	wildtype	dumbbell	87	
MDA-MB-436	wildtype	dumbbell	102	
MDA-MB-231	wildtype	dumbbell	185	we perform new experiments and include data adapted from [1]
MDA-MB-231	wildtype	rectangular	86	data adapted from [1]
MDA-MB-231	E-Cadherin transfection	dumbbell	63	
MDA-MB-231	GFP transfection	dumbbell	97	

Table 2: Overview over the various two-cell experiments conducted in this study. The column N indicates the number of trajectories extracted from the experiment.

cell line	perturbation	micropattern	N	comment
MCF10A	wildtype	dumbbell	215	data adapted from [2]
MCF10A	wildtype	rectangular	23	
MCF10A	E-Cadherin blocking	dumbbell	60	
MCF10A	EphrinA1	dumbbell	43	
MCF10A	TGF β	dumbbell	63	
A549	wildtype	dumbbell	100	
HT1080	wildtype	dumbbell	98	
MDA-MB-436	wildtype	dumbbell	102	
MDA-MB-231	wildtype	dumbbell	149	data adapted from [2]
MDA-MB-231	wildtype	rectangular	33	data adapted from [3]
MDA-MB-231	E-Cadherin transfection	dumbbell	45	
MDA-MB-231	GFP transfection	dumbbell	90	

Table 3: Overview over the various single cell experiments conducted in this study. The column N indicates the number of trajectories extracted from the experiment.

2.4 Experimental details of perturbations

In this section, we expand on experimental details of various molecular perturbations.

2.4.1 EMT in MCF10A cells

MCF10A cells were seeded in a T25 flask and treated with 10 ng/ml TGF β (Thermofisher) for 7 days. Every other day the medium was exchanged including TGF β . Western blot analysis shows the decrease in E-Cadherin expression and increase in N-Cadherin expression in TGF β -treated cells (figure S1a). In culture, TGF β -treated cells are more elongated and have a ruffled border at the edge compared to the untreated MCF10A cells (figure S1b).

2.4.2 mRNA construction

In this section, we give further details for the mRNA transfection of E-Cadherin into the breast cancer cell line MDA-MB-231.

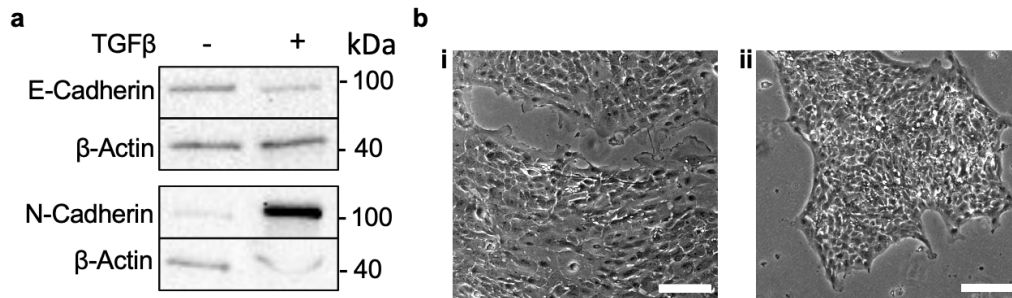


Figure S1: EMT in MCF10A. a) Western blot for E-Cadherin, N-Cadherin in untreated and TGF β -treated MCF10A cells. b) Brightfield images of TGF β -treated MCF10A cells (i) and untreated MCF10A cells (ii) after 7 days of culture.

1. Plasmid vector: hE-cadherin-pcDNA3 was a gift from Barry Gumbiner (Addgene plasmid #45769). The pSTI-A120-vector was a friendly gift from Dr. Carsten Rudolph (ethris GmbH) and has a 120-bp poly(A) tail and a 3' untranslated region (UTR) from human β -globin enabling in vitro transcription of polyadenylated RNA. To generate the desired vector, a Gibson DNA Assembly reaction was conducted by using the NEBuilder HiFi DNA Assembly kit (NEB, NEBuilder HiFi DNA Assembly Cloning Kit) as described. Briefly, the coding region for hE-cadherine was PCR amplified using the Q5 High-Fidelity PCR Kit (NEB). The oligonucleotide primers for the hE-cadherine-fragment were designed so that the DNA fragments to be assembled overlap each other by at least 30 bp at the ends.:

Primer (fwd): tacgactcactatagggcgaggagactgccaccATGGGCCCTTGGAGCCGC

Primer (rev): atctgcacgcctccttgcttgctgaattcGTGGTCCTCGCCGCCTCC)

The assembly reaction contained 100 pmol of insert DNA and 35 pmol of the SpeI-linearized pSTI-A120-vector and was incubated at 50°C for 20 min. After the GDA reaction was completed, the reaction mix was transformed into chemically competent E.coli cells (NEB 5-alpha Competent E. coli (High Efficiency), NEB). 100 μ L of the transformed LB (Lysogeny Broth)-E.coli-mix were plated onto LB/Kanamycin plates, followed by 37°C incubation overnight. Single colonies were picked and positive clones were further verified by DNA sequencing. To eliminate the SapI-restriction site in the hE-cadherine gene, we carried out a mutagenesis and exchange leucin to isoleucine by using Q5® Site-Directed Mutagenesis Kit (NEB) as described. Positive clones were verified by DNA sequencing.

2. mRNA production: To generate in vitro-transcribed mRNA (IVT RNA), the plasmid was linearized downstream of the poly(A) tail by SapI digestion and purified with the NEB Monarch PCR & DNA Cleanup Kit (NEB). The linearized vector (1 μ g) was used as a template for the in vitro transcription reaction using the Biozym Kit (MessageMAX™ T 7 ARCA-Capped Message Transcription Kit), having 100% of the Anti-Reverse Cap Analog in the produced IVT RNA in the correct orientation, increasing the translation efficiency of the IVT RNA. The complete IVT mix was incubated at 37°C for 45 min followed by a DNA digestion with DNaseI for 15 min at 37°C. RNA was precipitated with ammonium acetate and washed with 70% EtOH. The washing step was performed twice. Finally, the RNA pellet was re-suspended in RNase-free water.

3 Supplementary analysis of the experimental data

In this section, we describe supplementary analysis results of the experimental data that support the conclusions drawn in the main text.

3.1 Single cell behavior of the different cell types

An important aspect of two cells colliding is the way single cells migrate on their own. Thus, for all of our two-cell experiments, we additionally investigate single cells migrating on our dumbbell-shaped micropattern (Supplementary movie 2). Specifically, we track individual cells and analyze the statistical properties of the resulting cell trajectories. We will use knowledge about the single-cell behavior in three places: i) we show that our cells exhibit different levels of "invasiveness" in section 3.1.1. This reveals that our selection of cells covers invasive and non-invasive cell lines. ii) We investigate in section 5.6 the influence of single cell migration aspects on two-cell dynamics within our phenomenological model. iii) In section 3.1.3, we investigate how our molecular perturbations affect the single cell behavior of our cell lines.

3.1.1 Dynamics of single cell behavior of cell types

To quantify the single cell behavior of our considered cell types, we analyze how single cells transition between the two islands of our dumbbell-shaped geometry (Fig. S2a). Specifically, we track the cell nucleus (Fig. S2b) and find the steady-state probability distribution of the nucleus position. In agreement with [2], this pdf reveals that single cells prefer to be on one of the two islands of the dumbbell-shaped micropattern (Fig. S2c). In addition, we analyze the dynamical features of cell hopping. Specifically, we measure the survival probability of a cell $S(t)$. This is the probability that after a time t , the cell has not transitioned yet. We expect that this probability decays for all cell types as all cells show prominent hopping behavior (Fig. S2b) and thus it is less likely for cells to stay long on one island. Interestingly, we observe differences in the survival probability of the various different cell types. The two breast cancer cell lines (MDA-MB-231 and MDA-MB-436) as well as the fibrosarcoma cell line HT1080 exhibit lower survival probabilities than the epithelial (A549 and MCF10A) cell types. This indicates that breast cancer cell lines and the fibrosarcoma cell line transition more frequently and thus are more invasive than the epithelial cell lines. To gain more detailed insight into the dynamics of single cell behavior, we infer the dynamics of the nucleus using ULI (Methods). As no cell-cell interactions are present, we impose

$$\dot{v} = F_s(x, v) + \sigma \eta(t) \quad (\text{S1})$$

Here $F_s(x, v)$ describes the deterministic driving capturing how the nucleus of a single cell is on average accelerated at a given position and velocity like used in the main text. This effective driving force encodes how the migrating cell interacts with the geometric confinement of the micropattern and gives rise to the hopping dynamics. To capture the stochasticity of the cell trajectories, we include a dynamical noise term $\sigma \eta(t)$, where σ is the noise amplitude and $\eta(t)$ is a Gaussian white noise as defined in the Methods. We infer $F_s(x, v)$ and simulate our inferred equation of motion. The analysis of the simulated trajectories shows that the inferred effective force terms $F_s(x, v)$ capture the dynamics of hopping of all our cell types (dotted lines in Fig. S2c,d). Of note are that all (except the lung epithelial cells A549) deterministically accelerate as they move onto the bridge (red region at $v > 0$ and $x \approx 0$) (Fig. S2e). Taken together, these results show that our cells exhibit qualitatively similar underdamped hopping dynamics, but cell types have quantitatively distinct survival probabilities.

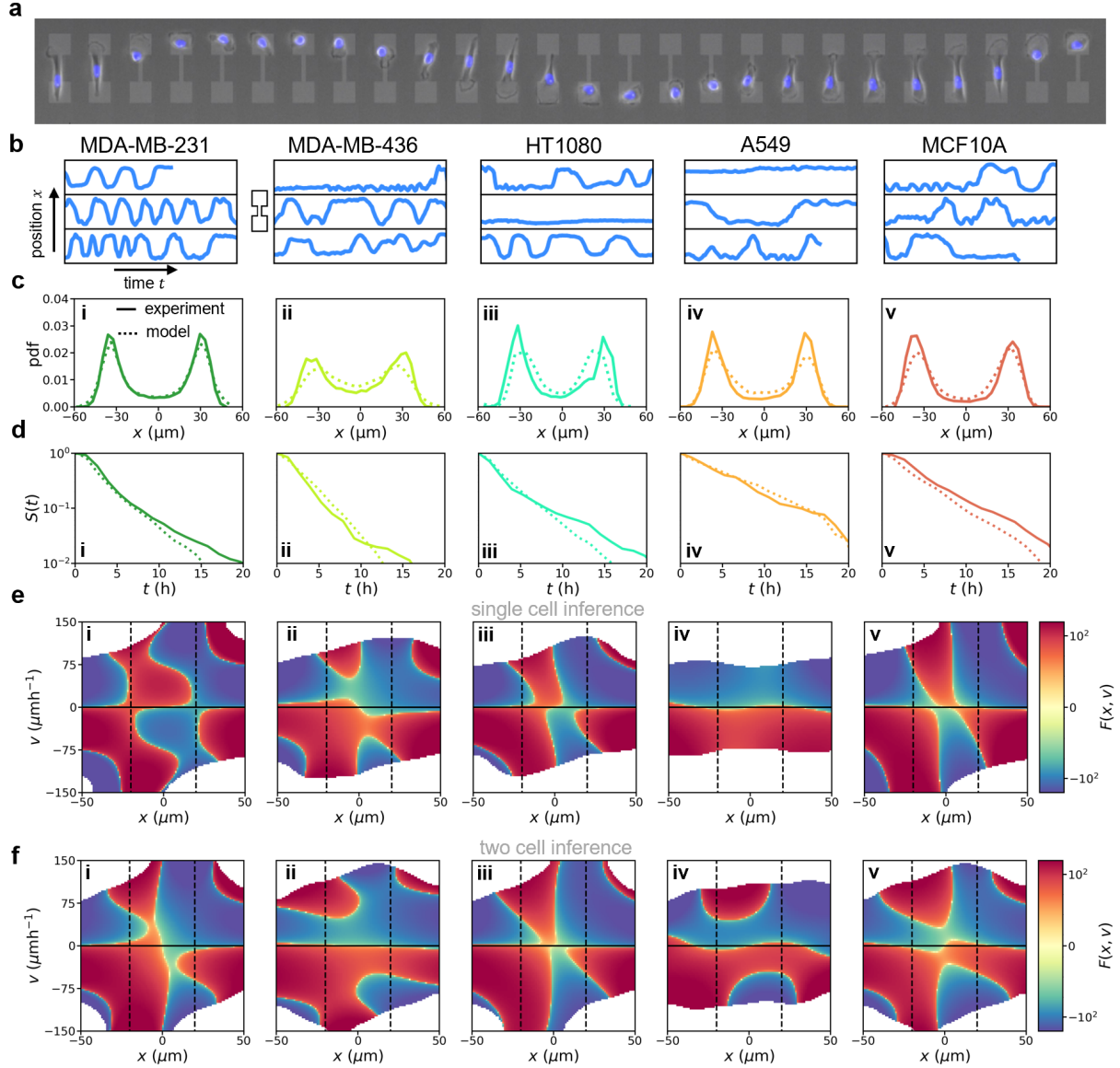


Figure S2: Underdamped dynamics of single cell behavior. **a)** Time series of brightfield images of a single MDA-MB-231 cell hopping between the two islands of our pattern. **b)** Small selection of nucleus trajectories for the five different cell lines. **c)** Steady state probability distribution of the position of the cell nucleus. **d)** Survival probability $S(t)$ for the five different cell types. Both in (c) and (d), solid lines show experimental results and dotted lines show model results obtained from simulating the inferred equation of motion S1. **e)** Inferred effective force $F(x, v)$ for all five cell types. $F_s(x, v)$ encodes the average acceleration of a cell nucleus given a certain position x and velocity v . Positive values indicates positive accelerations to right on our pattern. Vertical black dashed lines indicate the two islands separated by the bridge on our pattern. **f)** Inferred effective force $F(x, v)$ for all five cell types from our two-cell inference procedure.

3.1.2 Robustness of the single cell behavior

Here we investigate if the inferred single cell dynamics is altered in the presence of cell-cell interactions. To this end, we consider the single cell terms $F(x, v)$ that we infer from experimental data on two cells interacting as discussed in the main text. We show these single cell terms in Fig. S2f. Furthermore, we consider the inferred single cell terms $F_s(x, v)$ from our single cell analysis presented in section 3.1.1,

where we know that there are no cell-cell interactions involved in determining the nucleus dynamics of the cells. Thus, if the single cell behavior is unaffected by the presence of a second cell, we expect that $F_s(x, v) \approx F(x, v)$. A comparison of the two terms for each cell type (Fig. S2e,f) reveals that the single cell behavior of all our cell types is not significantly affected by the presence of cell-cell interactions with other cells.

3.1.3 Single cell behavior after perturbations

In this section, we analyze the impact of our molecular perturbations on the single cell behavior of our cell types. Specifically, we compare the inferred single cell dynamics $F_s(x, v)$ and the survival probability $S(t)$ of the wild type epithelial MCF10A and breast cancer MDA-MB-231 cells with their respective molecular perturbations. We find for MCF10A cells that for the anti-body blockings of E-Cadherin and EphrinA1 the inferred single cell dynamics $F_s(x, v)$ are qualitatively similar to the wild type (Fig. S3a i-iii). Furthermore, also the survival probability of the MCF10A cells is roughly similar to the MCF10A cells with anti-body blockings of E-Cadherin and EphrinA1 (Fig. S3b). For the TGF β treated cells, we find that the single cell dynamics changed and are qualitatively similar to that of cancerous MDA-MB-231 cells (Fig. S3a iv, c i) while the survival probabilities remain almost unchanged (Fig. S3b). For MDA-MB-231 cells we analyze the single cell behavior of our transfection experiment. We find that MDA-MB-231 cells with transfected GFP does neither greatly affect the single cell dynamics nor the survival probability of these cells (Fig. S3c,d). In contrast, the single cell behavior of MDA-MB-231 cells transfected with E-Cadherin does change to the single cell behavior observed in more epithelial A549 cells. Taken together, we show that antibody blockings do not greatly affect single cell behavior, but more complex perturbations like inducing EMT in MCF10A cells or transfecting MDA-MB-231 cells with E-Cadherin does change aspects of single cell behavior.

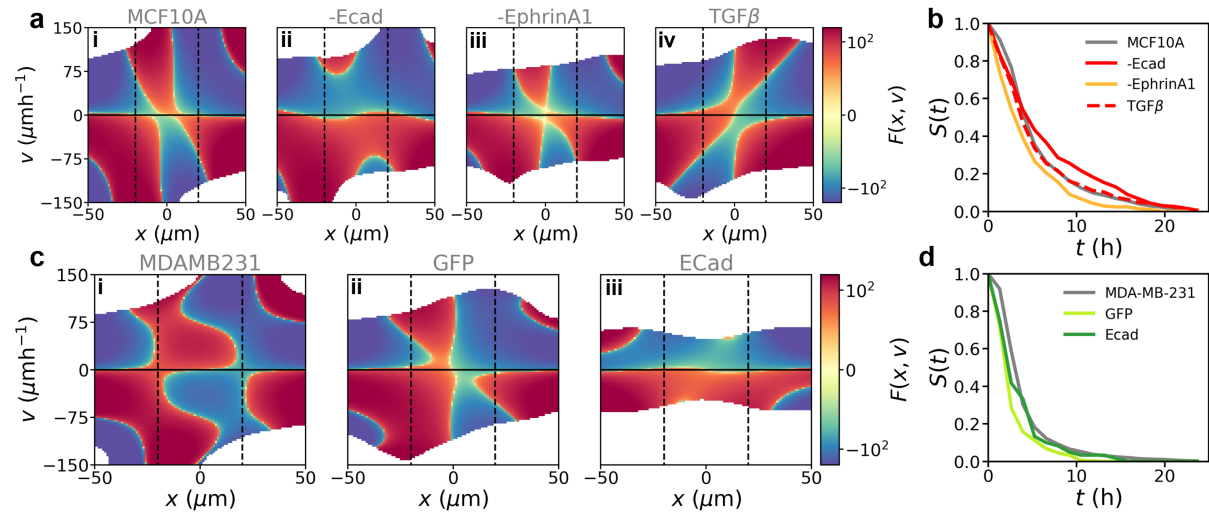


Figure S3: **Single cell behavior after molecular perturbations.** **a)** Inferred effective force $F(x, v)$ for wild type MCF10A cells (i) and the three considered molecular perturbations (ii-iv). $F_s(x, v)$ encodes the average acceleration of a cell nucleus given a certain position x and velocity v . Positive values indicates positive accelerations to right on our pattern. Vertical black dashed lines indicate the two islands separated by the bridge on our pattern. **b)** Survival probability $S(t)$ of MCF10A cells and the considered molecular perturbations. **c)** Inferred effective force $F(x, v)$ for wild type MDA-MB-231 cells (i) and the two transfected MDA-MB-231 cell lines (ii,iii). **d)** Survival probability $S(t)$ of MDA-MB-231 cells and the considered transfections.

3.2 Controlling E-Cadherin transfection

In this section, we compare the dynamics of wildtype MDA-MB-231 cells to MDA-MB-231 cells that have been transfected with GFP. We conducted this transfection in order to control the effects of the protocol that we used to transfect MDA-MB-231 cells with E-Cadherin. Analyzing the correlation functions of velocities and positions as well as the collision statistics as in the main text, we find that both wildtype MDA-MB-231 cells and GFP-transfected MDA-MB-231 cells exhibit very similar behavior statistics. Furthermore, we infer similar underdamped cohesion and friction interactions from the trajectories of these two cell types. Thus, we conclude that the transfection protocol does not greatly affect the two-cell dynamics of MDA-MB-231 cells.

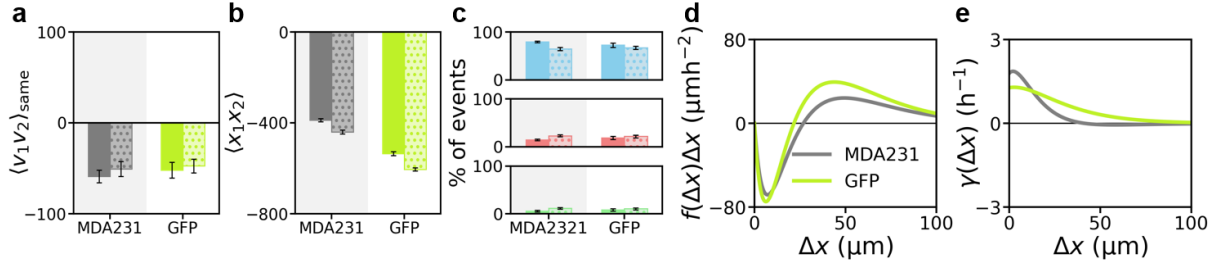


Figure S4: **Controlling the E-cadherin transfection.** **a)** Instantaneous velocity cross-correlation between the two cells when they occupy the same island. Solid bars show experimental results, dotted bars show the prediction of the inferred underdamped description. For panels (a)-(c), error bars show the error of the mean (s.e.m) obtained from bootstrapping. **b)** Instantaneous position cross-correlation between the two cells. **c)** Percentages of the three different collision events for the five different cell lines. **d)** Inferred effective cohesion interactions for the five different cell lines. Colors correspond to the two cell types as shown in panels (a) and (b). **f)** Inferred effective friction interactions for the five different cell lines.

3.3 Complete quantification of the experimental nucleus dynamics

In the main text, we only plot the instantaneous velocity correlation $C_V(|t - t'| = 0)$ and the instantaneous position correlation $C_X(|t - t'| = 0)$. In Fig. S5 we show the full result of these behavior statistics and show also long time scale correlations of the various cell types. Also these long time scale correlations are well captured by the inferred Langevin equation (red curves in Fig. S5c,d).

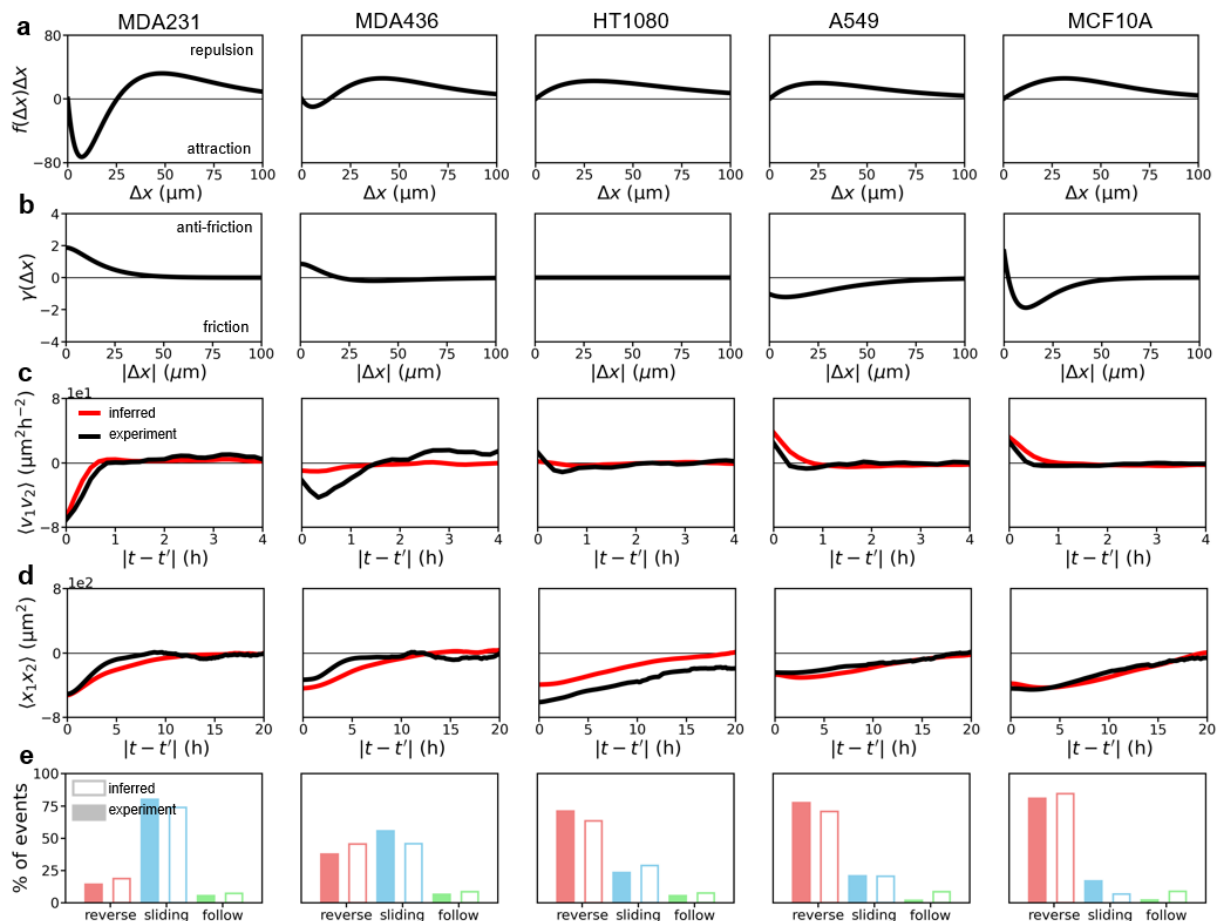


Figure S5: **Behavior statistics and inferred interactions for all cell types** a),b) Underdamped cohesion (a) and friction (b) interactions for all cell types c)-e) Behavior statistics for all cell types. Black curve shows experimental results, red curves show the behavior predicted by the inferred langevin equation including the underdamped interactions shown in panels (a) and (b). Here, (c) shows the velocity correlation function $\langle v_1(t)v_2(t') \rangle_{\text{same}}$ when cells are on the same island. (d) show the position correlation function $\langle x_1(t)x_2(t') \rangle$. (e) shows the collision statistics for all different cell types.

4 Model development and fitting procedure

In this section, we expand on details of the development and implementation of the phenomenological model for cell-cell interactions used in the main text to capture the interaction behavior of various different cell types.

4.1 Model definition

We model cells as generalized spatially extended active particles [3] confined to move in 1D on a dumbbell-shaped geometry. In the model, we describe the overdamped dynamics of the position of the cell nucleus $x_{n,i}$, the position of the cell's protrusion $x_{p,i}$, and the stochastic dynamics of cell polarity P_i , where i indicates cell i :

$$\dot{x}_{n,i} = -\frac{k_n}{\gamma(x_{n,i})}(x_{n,i} - x_{p,i}) + G_n(\Delta x, P, \Delta P) \quad (\text{S2})$$

$$\dot{x}_{p,i} = k_p(x_{n,i} - x_{p,i}) + P_i(t) + G_p(\Delta x, P, \Delta P) + F_{\text{boundary}}(x_{p,i}) \quad (\text{S3})$$

$$\dot{P}_i = -\alpha(x_{p,i})P_i - \beta P_i^3 + G_P(\Delta x, P, \Delta P) + \sigma \eta_i(t) \quad (\text{S4})$$

Here, the nucleus and the protrusion of the same cell are coupled by a linear spring and $k_n = k/\zeta_n$ and $k_p = k/\zeta_p$ are the spring constants reduced by the friction coefficients of the cell nucleus ζ_n and the cell protrusion ζ_p respectively. Furthermore, $\gamma(x_{n,i})$ is a dimensionless rescaling factor of the friction coefficient ζ_n that depends on the position of the cell nucleus with a minimum when the cell nucleus is on the bridge. This models the reduced adhesive area accessible to the cell on the bridge, which is a key feature of confined cell migration on our pattern [3]. Following [3], we choose

$$\gamma(x_{n,i}) = \frac{1 - \gamma_{\min}}{2} \left(1 - \cos \left(\frac{x_{n,i}\pi}{L_{\text{system}}} \right) \right) + \gamma_{\min} \quad (\text{S5})$$

where L_{system} is the half of the size of the dumbbell-shaped micropattern and γ_{\min} is the minimum rescaling factor reached while the nucleus is on the bridge (Fig. S6a). The cell's protrusion is confined on the micropattern by a boundary force $F_{\text{boundary}}(x_{p,i})$, which represents a soft repulsive force at the boundaries of the micropattern. In this model, the polarity dynamics of the cell is guided by the geometry of the micropattern [3]. This is implemented by the function $\alpha(x_{p,i})$, which switches sign dependent on $x_{p,i}$ (Fig. S6b):

$$\alpha(x_{p,i}) = -\frac{\alpha_0 - \alpha_{\min}}{2} \cos \left(\frac{x_{p,i}\pi}{L_{\text{sys}}} \right) + \frac{\alpha_{\min} + \alpha_0}{2} \quad (\text{S6})$$

where $\alpha(x_{p,i}) = \alpha_0$ on the island and $\alpha(x_{p,i}) = \alpha_{\min} < 0$ on the bridge. The higher order term $-\beta P^3$ in equation S4 prevents unbounded growth of the polarity and gives rise to a preferred polarity when $\alpha(x_{p,i})$ is negative. These single cell aspects of our model can be derived from a microscopic model for migrating cells [4]. Throughout the paper, we make use of a set of parameters ($\sigma = 100 \mu\text{mh}^{-\frac{1}{2}}$, $k_n = 0.6 \text{ h}^{-1}$, $k_p = 1.2 \text{ h}^{-1}$, $\beta = 0.0001 \mu\text{m}^{-2}\text{h}$, $\alpha_0 = 10 \text{ h}^{-1}$, $\alpha_{\min} = -6 \text{ h}^{-1}$, $\gamma_{\min} \approx 0.25$, $L_{\text{system}} = 52.5 \mu\text{m}$) which has been constrained for MDA-MB-231 cells using a data-driven inference approach and best describes the detailed dynamics of the hopping behavior of single MDA-MB-231 cells on the dumbbell-shaped

micropattern used here [3]. In section 5.6, we describe how these parameters vary across cell types and investigate the role of single cell aspects on the interaction dynamics of cells.

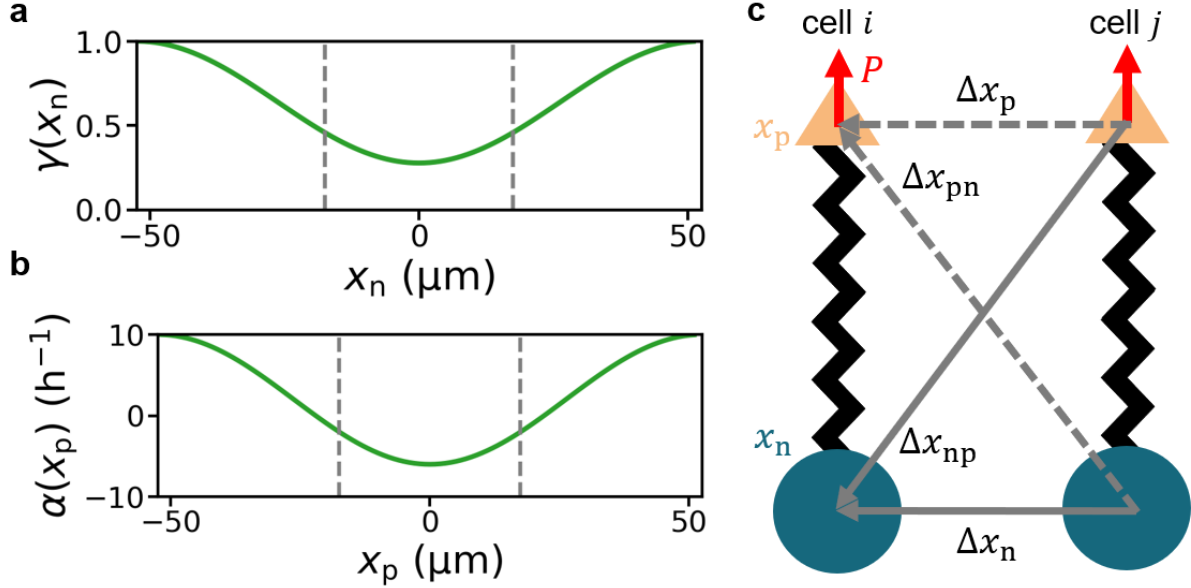


Figure S6: **Details of our phenomenological model.** **a)** Rescaling factor $\gamma(x_{n,i})$ used in our phenomenological model. Vertical dashed lines indicate the boundary of the two islands and the bridge of our dumbbell shaped micropattern. **b)** Geometry-dependent growth rate of the polarity $\alpha(x_{p,i})$ in our phenomenological model. **c)** Schematic of two cells in our model and all vectorial quantities that we can use to construct cell-cell interactions.

Finally, G_n , G_p , and G_P are generic interaction terms that can depend on the four interparticle distances $\Delta x_n = x_{n,i} - x_{n,j}$, $\Delta x_{np} = x_{n,i} - x_{p,j}$, $\Delta x_{pn} = x_{p,i} - x_{n,j}$, $\Delta x_p = x_{p,i} - x_{p,j}$, cell polarities P_i , P_j , and differences in polarity $\Delta P = P_i - P_j$ (Fig. S6c). In the next subsections, we systematically define terms encoding interaction mechanisms.

4.2 Overview of model strategy

To develop a phenomenological model for cell-cell interactions we employ the following strategy: First, we define the interaction terms G_n , G_p , and G_P in a systematic and unbiased way based on symmetry and simplicity arguments. We then perform numerical simulations of the equations of motion for each candidate interaction term and measure the behavior statistics and infer the underdamped interaction terms using underdamped Langevin inference (ULI) [5]. We then analyze qualitatively these dynamics in section 5.1.1. Afterwards, we perform a fit of the the phenomenological model with each candidate interaction term to the experimental data as described in section 4.5. The goal of the fit is to minimize the deviations of the inferred underdamped interactions and behavior statistics of the phenomenological model to the inferred underdamped interactions and behavior statistics of the experimental data. In the end, we select the best performing cell-cell interaction term based on how good that term can be fitted to the experimental dynamics.

4.3 Complete description of cell-cell interaction mechanisms

First, we discuss how we construct candidate cell-cell interaction terms in an unbiased and systematic way. To this end, we assume (i) that our model obeys rotational and translational symmetry. Thus, cell-cell interactions in our model can not depend on the absolute position of cells and can only depend on quantities in our model that behave as vectors in arbitrary dimensions. These quantities are $\Delta x_n = x_{n,i} - x_{n,j}$, $\Delta x_{np} = x_{n,i} - x_{p,j}$, $\Delta x_p = x_{p,i} - x_{p,j}$, $\Delta x_{pn} = x_{p,i} - x_{n,j}$, P_i , P_j , and $\Delta P = P_i - P_j$ (Fig. S6c). We furthermore exclude interactions that depend on time derivatives of these vectorial quantities. This is because we assume that our overdamped equations of motion describe how the friction of the cells is balanced by all forces that act on the cells. Thus, time derivatives can only appear on the left hand side of our equations. In principle, G_n , G_p , and G_P may depend in a complicated way on the four vectorial quantities. Instead of proposing very specific functional dependencies, we employ a minimal approach and propose (ii) interaction terms that are linear in the vectorial quantities. Furthermore, we impose a characteristic interaction range by assuming that (iii) interactions exponentially decay on a length scale r . This means that cells that are sufficiently separated do not significantly interact in our model. This leaves us with the following functional dependencies that we can use to construct cell-cell interaction terms:

$$\varepsilon e^{-|\Delta x|/r} \Delta x \quad (S7)$$

$$\varepsilon e^{-|\Delta x|/r} P \quad (S8)$$

$$\varepsilon e^{-|\Delta x|/r} \Delta P \quad (S9)$$

Here, ε is the interaction strength in our phenomenological model and Δx is either Δx_n , Δx_{np} , Δx_p or Δx_{pn} . Also P is either equal to P_i or P_j . From these expressions, we construct possible cell-cell interaction mechanisms. Before doing so, we have to specify the dependencies of the interaction terms G_n , G_p , and G_P . To this end, we assume (iv) that interactions do not introduce additional coupling between the degrees of freedom that are not already introduced by the single cell terms. This means that for instance $\dot{x}_{n,i}$ shouldn't explicitly be influenced by terms that depend on the relative separation of the two protrusions Δx_p . Such a dependency would couple the nucleus of cell i with the protrusion of cell i in an additional way to the already introduced linear coupling. In practice, this means that G_n can only depend on Δx_n , Δx_{np} , and P_j . Furthermore, G_p only depends on Δx_p , Δx_{pn} , or P_j . This assumption then also implies that G_P can only depend on P_i , P_j or ΔP . However, note that P is an internal degree of freedom and not a positional degree of freedom like x_n and x_p . Thus, in order to fulfill the assumption that interactions decay in space, we allow G_P to depend on Δx_p or Δx_{pn} even though this introduces an additional coupling. In summary, we make the following assumptions:

1. Rotational and translational symmetry
2. Linearity for simplicity
3. Exponential decay of the interaction strength
4. No additional single cell couplings (relaxed for the polarity interactions to allow for exponential decay of the interaction strength)

The resulting cell-cell interaction mechanisms include the following couplings:

- **NC** (nucleus coupling): $G_n(\Delta x_n) = \varepsilon_{NC} e^{-|\Delta x_n|/r_{NC}} \Delta x_n$, modeling either repulsion ($\varepsilon_{NC} > 0$) or attraction ($\varepsilon_{NC} < 0$) interactions between the cell nuclei.

- **NPrC** (nucleus-protrusion coupling): $G_n(\Delta x_{np}) = \epsilon_{\text{NPrC}} e^{-|\Delta x_{np}|/r_{\text{NPrC}}} \Delta x_{np}$, modeling either repulsion ($\epsilon_{\text{NPrC}} > 0$) or attraction ($\epsilon_{\text{NPrC}} < 0$) interactions between the cell nucleus and the protrusion of the other cell.
- **NPC** (nucleus-polarity coupling): $G_n(\Delta x_{np}, P_j) = \epsilon_{\text{NPC}} e^{-|\Delta x_{np}|/r_{\text{NPC}}} P_j$, modeling a potential direct influence of the polarity of cell j on the nucleus position of cell i . For $\epsilon_{\text{NPC}} < 0$, we have that the nucleus reacts opposite to the polarity of the other cell.
- **PrC** (protrusion coupling): $G_p(\Delta x_p) = \epsilon_{\text{PrC}} e^{-|\Delta x_p|/r_{\text{PrC}}} \Delta x_p$, modeling either repulsion ($\epsilon_{\text{PrC}} > 0$) or attraction ($\epsilon_{\text{PrC}} < 0$) interactions between the cell protrusions.
- **PrNC** (protrusion-nucleus coupling): $G_p(\Delta x_{pn}) = \epsilon_{\text{PrNC}} e^{-|\Delta x_{pn}|/r_{\text{PrNC}}} \Delta x_{pn}$, modeling either repulsion ($\epsilon_{\text{PrNC}} > 0$) or attraction ($\epsilon_{\text{PrNC}} < 0$) interactions between the cell protrusion and the nucleus of the other cell.
- **PrPC** (protrusion-polarity coupling): $G_p(\Delta x_{pn}, P_j) = \epsilon_{\text{PrPC}} e^{-|\Delta x_{pn}|/r_{\text{PrPC}}} P_j$, modeling a direct influence of the polarity of cell j on the protrusion of cell i . For $\epsilon_{\text{PrPC}} < 0$, we have that the protrusion reacts opposite to the polarity of the other cell.
- **PPrC** (polarity-protrusion coupling): $G_p(\Delta x_p) = \epsilon_{\text{PPrC}} e^{-|\Delta x_p|/r_{\text{PPrC}}} \Delta x_p$ models that the growth rate of the polarity is dependent on the separation between the cell protrusions as well as on the orientation of cells with respect to each other. For $\epsilon_{\text{PPrC}} > 0$, the polarity grows away from the protrusion of the other cell while for $\epsilon_{\text{PPrC}} < 0$, the polarity grows towards the other protrusion. Note that this interaction has been used to model contact inhibition of locomotion [6].
- **PNC** (polarity-nucleus coupling): $G_p(\Delta x_{pn}) = \epsilon_{\text{PNC}} e^{-|\Delta x_{pn}|/r_{\text{PNC}}} \Delta x_{pn}$ models that the growth rate of the polarity is dependent on the separation between the cell's protrusion and the other cell's nucleus. For $\epsilon_{\text{PNC}} < 0$, the polarity grows towards the other nucleus.
- **PSC** (polarity self coupling): $G_p(\Delta x_p, P_i) = -\epsilon_{\text{PSC}} e^{-|\Delta x_p|/r_{\text{PSC}}} P_i$. This interaction models the polarity shrinking (or growing dependent on the sign of ϵ_{PSC}) dependent on the relative separation between cells but irrespective of the relative orientations of the cells.
- **PCC** (polarity cross coupling): $G_p(\Delta x_p, P_j) = \epsilon_{\text{PCC}} e^{-|\Delta x_p|/r_{\text{PCC}}} P_j$. This interaction is mathematically very similar to PSC, but now the shrinking of polarity P_i is not set by P_i but instead it depends on P_j . This interaction thus models how the polarity of cell i grows or shrinks with at rate given by the polarity of cell j . Here $\epsilon_{\text{PCC}} > 0$ indicates polarity growth. Note that this interaction has been called an alignment interaction in the literature [6].
- **PPC** (polarity-polarity coupling) $G_p(\Delta x_p, \Delta P) = -\epsilon_{\text{PPC}} e^{-|\Delta x_p|/r_{\text{PPC}}} \Delta P$, which models the cell's polarity aligning to the polarity of the other cell dependent on the relative separation between the cell protrusions. For $\epsilon_{\text{PPC}} < 0$, we have anti-alignment of cell polarity. Note that PPC and PCC both describe how the polarity of cell i grows dependent on the polarity of cell j . The difference between these interactions is only given by the final polarities after interacting. In the case of PPC, growth stops when cells minimize ΔP . In the case of PCC, growth is stopped by the non-linear term $-\beta P^3$.

We summarize all the interactions in table 4. Altogether, this yields a large amount of unbiased candidate interactions.

candidate interaction	abbreviation	term	equation
nucleus coupling	NC	G_n	$\epsilon_{NC} e^{- \Delta x_n /r_{NC}} \Delta x_n$
nucleus-protrusion coupling	NPrC	G_n	$\epsilon_{NPrC} e^{- \Delta x_{np} /r_{NPrC}} \Delta x_{np}$
nucleus-polarity coupling	NPC	G_n	$\epsilon_{NPC} e^{- \Delta x_{np} /r_{NPC}} P_j$
protrusion coupling	PrC	G_p	$\epsilon_{PrC} e^{- \Delta x_p /r_{PrC}} \Delta x_p$
protrusion-nucleus coupling	PrNC	G_p	$\epsilon_{PrNC} e^{- \Delta x_{pn} /r_{PrNC}} \Delta x_{pn}$
protrusion-polarity coupling	PrPC	G_p	$\epsilon_{PrPC} e^{- \Delta x_{pn} /r_{PrPC}} P_j$
polarity-protrusion coupling	PPrC	G_p	$\epsilon_{PPrC} e^{- \Delta x_p /r_{PPrC}} \Delta x_p$
polarity-nucleus coupling	PNC	G_p	$\epsilon_{PNC} e^{- \Delta x_{pn} /r_{PNC}} \Delta x_{pn}$
polarity self coupling	PSC	G_p	$\epsilon_{PSC} e^{- \Delta x_p /r_{PSC}} P$
polarity cross coupling	PCC	G_p	$\epsilon_{PCC} e^{- \Delta x_p /r_{PCC}} P_j$
polarity-polarity coupling	PPC	G_p	$\epsilon_{PPC} e^{- \Delta x_p /r_{PPC}} \Delta P$
pol.-prot. coupling + nucleus coupling	PPrC+NC	G_p G_n	$\epsilon_{PPrC} e^{- \Delta x_p /r_{PPrC}} \Delta x_p$ $\epsilon_{NC} e^{- \Delta x_n /r_{NC}} \Delta x_n$
pol. coupling + pol. self coupling	PPC+PSC	G_p	$\epsilon_{PPC} e^{- \Delta x_p /r_{PPC}} \Delta P$ + $\epsilon_{PSC} e^{- \Delta x_p /r_{PSC}} P$
pol. coupling + prot. coupling	PPC+PrC	G_p G_p	$\epsilon_{PPC} e^{- \Delta x_p /r_{PPC}} \Delta P$ $\epsilon_{PrC} e^{- \Delta x_p /r_{PrC}} \Delta x_p$
pol. coupling + pol.-nucl. coupling	PPC+PNC	G_p	$\epsilon_{PPC} e^{- \Delta x_p /r_{PPC}} \Delta P$ + $\epsilon_{PNC} e^{- \Delta x_{pn} /r_{PNC}} \Delta x_{pn}$
pol. coupling + pol.-prot. coupling	PPC+PPrC	G_p	$\epsilon_{PPC} e^{- \Delta x_p /r_{PPC}} \Delta P$ + $\epsilon_{PPrC} e^{- \Delta x_p /r_{PPrC}} \Delta x_p$

Table 4: Summary of all candidate cell-cell interactions. The column "term" indicates in which of the three interaction terms in the overdamped equations of motion we add the candidate interaction.

4.4 Model implementation

We numerically solve equations S2 - S4 by a Euler-Maruyama forward integration scheme. To this end, we initialize random positions for the cell nucleus on the pattern and choose close but random positions of the protrusion. The polarity of cells is also randomly initialized. For each candidate interaction we then simulate $N = 3000$ timesteps with a time step of $dt = 1/60$ h. We oversample and only retain every 10th timestep to obtain a final simulation time of $T = 50$ h with a timedelta of $\Delta t = 1/6$ h. These values are similar to the experimental values. These numerical simulations yield the model nucleus trajectories shown in main text Fig. 4c and are analyzed in a similar way like the experimental data.

4.5 Model fitting

To fit our phenomenological model to the experimental data, for each candidate cell-cell interaction, we vary the set of parameters Θ in our model and numerically simulate $N = 150$ two-cell trajectories. Here Θ consists out of ε and r for the respective candidate interaction. Note that if we combine candidate cell-cell interactions, we have four parameters in Θ . We then infer the underdamped cell-cell interactions and measure the behavior statistics predicted by our phenomenological model. In the following, we lay out how we fit our phenomenological model to the experimental data. We then show the results of the fitting procedure including a comprehensive comparison of our candidate interactions in section 5.1.

4.5.1 The coefficient of determination

To quantify the goodness of fit to the experimental data, we compute the so called *coefficient of determination* (COD), which is defined as

$$R^2 = 1 - \frac{SS_{res}}{SS_{tot}} \quad (\text{S10})$$

Here, SS_{res} is defined as the sum of the squared deviations between the model and the experiment:

$$SS_{res} = \sum_i (y_i - \hat{y}_i)^2 \quad (\text{S11})$$

with \hat{y} being either the model result for the underdamped cohesion interaction $f(\Delta x)\Delta x$, the underdamped friction interaction $\gamma(\Delta x)$ or one of the three behavior statistics we employ in the main text. Here, y is the experimental results and the index i indicates the discrete positions/categories where the statistics are measured. SS_{tot} is then the variance of the experimental data:

$$SS_{tot} = \sum_i (y_i - \bar{y}_i)^2 \quad (\text{S12})$$

R^2 is equal to 1 if the model matches the experiment so that $SS_{res} = 0$. Furthermore, R^2 is around 0 if the model predicts at least the mean of the experimental data \bar{y} and negative if the model does worse than that. Varying all parameters in the model gives the COD as a function of the model parameters for each candidate cell-cell interaction, for each cell type and for each statistics: $R_{j,k}^2(\Theta)$. Here j indicates the statistics of which we want to assess the goodness of fit. So $R_{d,k}^2(\Theta)$ indicates the COD of the model fit to the underdamped interactions, while $R_{v,k}^2(\Theta)$ and $R_{x,k}^2(\Theta)$ is the COD of capturing the correlation functions of the velocities and positions, respectively. $R_{c,k}^2(\Theta)$ is the COD of the collision statistics. The index k indicates different cell types.

4.5.2 Individual fit of the dynamics

To fit the dynamics, we need to maximize the COD for each cell type and across the various different statistics. Let's define

$$R_k^2(\Theta) = \langle R_{j,k}^2(\Theta) \rangle_j \quad (\text{S13})$$

as the mean COD across all our statistics for one individual cell type. Note, that we put equal weight on all the statistics. However, we exclude $R_{x,k}^2(\Theta)$ of the position correlations as we later will check if our

model can consistently predict one of the statistics. We first maximize R_k^2 individually for the different cell types without any constraints on the parameters. Thus, for each candidate cell-cell interaction, we find a unique set of parameters for each cell type as:

$$\hat{\Theta}_k = \arg \max_{\Theta} R_k^2(\Theta) \quad (\text{S14})$$

with

$$\hat{R}_k^2 = \max_{\Theta} R_k^2(\Theta) \quad (\text{S15})$$

To compare models, we plot \hat{R}_k^2 for each candidate interaction mechanism in main text Fig. 5a. We show in Fig. S14 the results of that procedure for each cell type for the best fitting candidate cell-cell interaction PPC+PPrC.

4.5.3 Global fit of the dynamics

Because we want to further challenge our theory and test if we can find a model that captures the experimental data with less parameters than the individual fit, we attempt a global fit of all cell types. Specifically, we try to capture the dynamics of all different cell lines with a single candidate interaction, while varying only a single parameter. This single parameter then has to tune between all the different behaviors that we observe in the experiment. For the single candidate cell-cell interactions we keep the interaction range r fixed and vary ε as we observed that in contrast to the interaction range, ε significantly affects the resulting dynamics. To this end, for each candidate interaction, we first vary ε and maximize the COD for each individual cell type for each value of r :

$$\hat{\varepsilon}_k(r) = \arg \max_{\varepsilon} R_k^2(\varepsilon, r) \quad (\text{S16})$$

this leaves us with optimal $\hat{\varepsilon}_k(r)$ for each cell type and each value of r . Then, for the global fit, we consider the COD at the optimal $\hat{\varepsilon}_k$ for each cell type:

$$\hat{R}_k^2(r) = \max_{\varepsilon} R_k^2(\varepsilon, r) \quad (\text{S17})$$

Note that in equation S15, \hat{R}_k^2 is a scalar, while \hat{R}_k^2 is a function of r in equation S17. We then average over different cell types to obtain a global COD defined as

$$\mathcal{R}^2(r) = \langle \hat{R}_k^2(r) \rangle_k \quad (\text{S18})$$

Finally, we maximize $\mathcal{R}^2(r)$ to obtain

$$\hat{r} = \arg \max_r \mathcal{R}^2(r) \quad (\text{S19})$$

with maximal global COD

$$\hat{\mathcal{R}}^2 = \max_r \mathcal{R}^2(r) = \max_r \langle \max_{\varepsilon} R_k^2(\varepsilon, r) \rangle_k \quad (\text{S20})$$

This gives us for each cell type a pair of parameters $(\hat{\varepsilon}_k(\hat{r}), \hat{r})$ with fixed \hat{r} . Thus, in this global fit, we effectively only use two parameters to capture the experimental data compared to the 10 parameters in the individual fit. In addition, for the pairs of interactions, we always allow the polarity-polarity-coupling strength ε_{PPC} to vary, while keeping all the other parameters (the interaction strength of the other interaction ε and the two interaction ranges for the two candidate interactions) fixed. This gives us a global COD $\mathcal{R}^2(\varepsilon, r_{\text{PPC}}, r)$, where ε and r are the strength and range of the other interaction. Finally, of important note is that for all candidate interactions we sweep over the parameter ranges in which we can identify at least a local maximum in the COD (Fig. S7). This way we make sure that the phenomenological model with all interaction mechanisms provides the best possible fit to the experimental data.

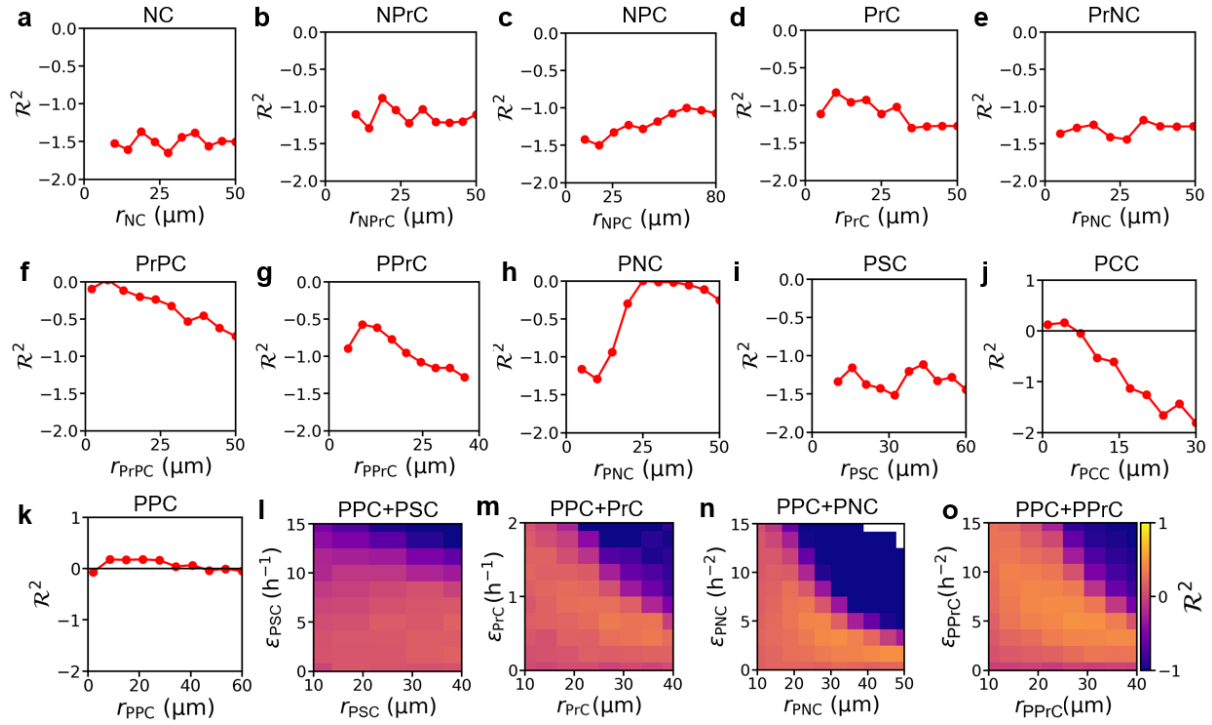


Figure S7: Coefficient of determination of the different candidate cell-cell interactions. a)-k) Coefficient of determination $\mathcal{R}^2(r)$ as determined in equation S18 for the 11 different candidate cell-cell interactions as a function of the interaction range. l)-o) Again the coefficient of determination $\mathcal{R}^2(r)$ for all the combined candidate cell-cell interactions. As we have three parameters in these combined models which we vary, we now show $\mathcal{R}^2(\epsilon_{rep}, r_{rep})$ where we vary the strength and range of the additional repulsion interaction that we add to polarity alignment interactions.

5 Supplementary model results

In this SI section we describe supplementary model results that support the conclusions drawn in the main text.

5.1 Comparing the dynamics of candidate cell-cell interactions

In this subsection, we show a detailed analysis and subsequent comparison of the underdamped nucleus dynamics that all our candidate cell-cell mechanisms predict.

5.1.1 Underdamped dynamics of candidate cell-cell interactions

To this end, we first discuss qualitative features of the various candidate cell-cell interactions. Specifically, we will analyze what underdamped cell-cell interactions and what behavior statistics the candidate cell-cell interactions can predict. For visualization and to show the best possible model predictions, we fix the interaction range r to \hat{r} , which is the value for the interaction range that provides the best global fit to the underdamped dynamics and behavior statistics of all cell types as defined in equation S19. For each candidate interaction we then vary the interaction strength ϵ . While doing so, we infer the underdamped cell-cell interactions and infer the various behavior statistics. We note that in the experiments, we observed strong correlations between the various behavior statistics and inferred interactions. Specifically, in the experiment we observed the combinations (Fig. S5):

- **cohesion, friction, positive** velocity correlations, **negative** position correlations, and dominant **reversal** behavior (in epithelial cells)
- **attraction, anti-friction, negative** velocity correlations, **negative** position correlations, and dominant **sliding** behavior (in breast cancer cells)

In the following, we summarize qualitative features of the various candidate cell-cell interaction mechanisms and discuss them in relation to the experimental data.

NC and NPrC: For both nucleus coupling and nucleus protrusion coupling, we find that our phenomenological model predicts both repulsive and attractive underdamped interactions, but is unable to predict significant anti-friction interactions (NC and NPrC in Fig. S8a,b). Furthermore, both candidates do not predict negative velocity correlations at short time scales (NC and NPrC in Fig. S8c) and thus are unable to capture both combinations as outlined above. However, these candidate interactions do predict mutual exclusion behavior and dominant reversal and sliding behavior (NC and NPrC in Fig. S8d,e).

NPC: For nucleus polarity coupling, we find very weak underdamped repulsion for ($\epsilon > 0$) but strong short-range repulsion and long-range attraction interactions for ($\epsilon < 0$) (NPC in Fig. S8a). This candidate cell-cell interaction is able to predict both friction and anti-friction (NPC in Fig. S8b). However, note that here strong short-range repulsion interactions are correlated with anti-friction, which we do not observe in the experimental data. Also this candidate interaction is able to predict both negative and positive velocity correlations and the switch from sliding behavior to reversal behavior (NPC in Fig. S8c,e).

PrC and PrNC: For protrusion coupling and protrusion nucleus coupling, we find very similar dynamics. We find that our models predicts significant underdamped repulsion and attraction interactions, but no significant underdamped anti-friction interactions (PrC and PrNC in Fig. S8a,b). Also, neither PrC nor PrNC are able to predict negative velocity correlations at short time scales (PrC and PrNC in Fig. S8c). Furthermore, PrC does not predict dominant sliding behavior while PrNC does (PrC and PrNC in Fig. S8e).

PrPC: For protrusion polarity coupling, we find repulsion and long range attraction interactions not observed in the experimental data (PrPC in Fig. S8a). We furthermore observe strong underdamped friction and anti-friction interactions (PrPC in Fig. S8b) and both positive and negative velocity correlations (PrPC in Fig. S8c). PrPC is unable to predict mutual exclusion behavior and does not give rise to dominant sliding events (PrPC in Fig. S8d,e).

PPrC: For polarity protrusion coupling, we observe a switch from short-range repulsion and long-range attraction to short-range attraction and long-range repulsion (PPrC in Fig. S9a). Here, repulsion interactions are correlated with anti-friction. In general, PPrC predicts dynamics that are very similar to PrC. Both mechanisms do not capture the correlations of the various behavior statistics and underdamped interactions as observed in the experimental data.

PNC: For polarity nucleus coupling, we find clear repulsion and attraction interactions, but no friction interactions (PNC in Fig. S9a,b). While this candidate cell-cell interaction is able to predict mutual exclusion behavior and both reversal and sliding behavior, it is unable to capture significant positive velocity correlations at short time scales (PNC in Fig. S9c-e).

PSC: For polarity self coupling, we find weak underdamped repulsion interactions and very weak underdamped anti-friction interactions (PSC in Fig. S9a,b). Furthermore, PSC does not predict negative velocity or position correlations, but is able to capture a switch from dominant sliding behavior to dominant reversal behavior (PSC in Fig. S9c-e).

PCC: For polarity cross coupling, we find that our model predicts a switch from short-range repulsion and long-range attraction to short-range attraction and long-range repulsion (PCC in Fig. S9a). Furthermore, repulsion interactions are correlated with friction interactions and attraction interactions are correlated with anti-friction interactions (PCC in Fig. S9a,b) as observed in the experimental data. PCC is able to predict both negative and positive velocity correlations as well as both sliding and reversal behavior (PCC in Fig. S9c-e).

PPC: Finally, for polarity alignment interactions, we observe a switch from repulsion and friction to attraction and anti-friction (PPC in Fig. S9a,b). Furthermore, PPC can predict a switch from positive to negative velocity correlations and a switch from dominant reversal to dominant sliding behavior (PPC in Fig. S9c,e). However, note that PPC is unable to predict pronounced position correlations (PPC in Fig. S9d). Thus, PPC does not lead to mutual exclusion behavior of cells.

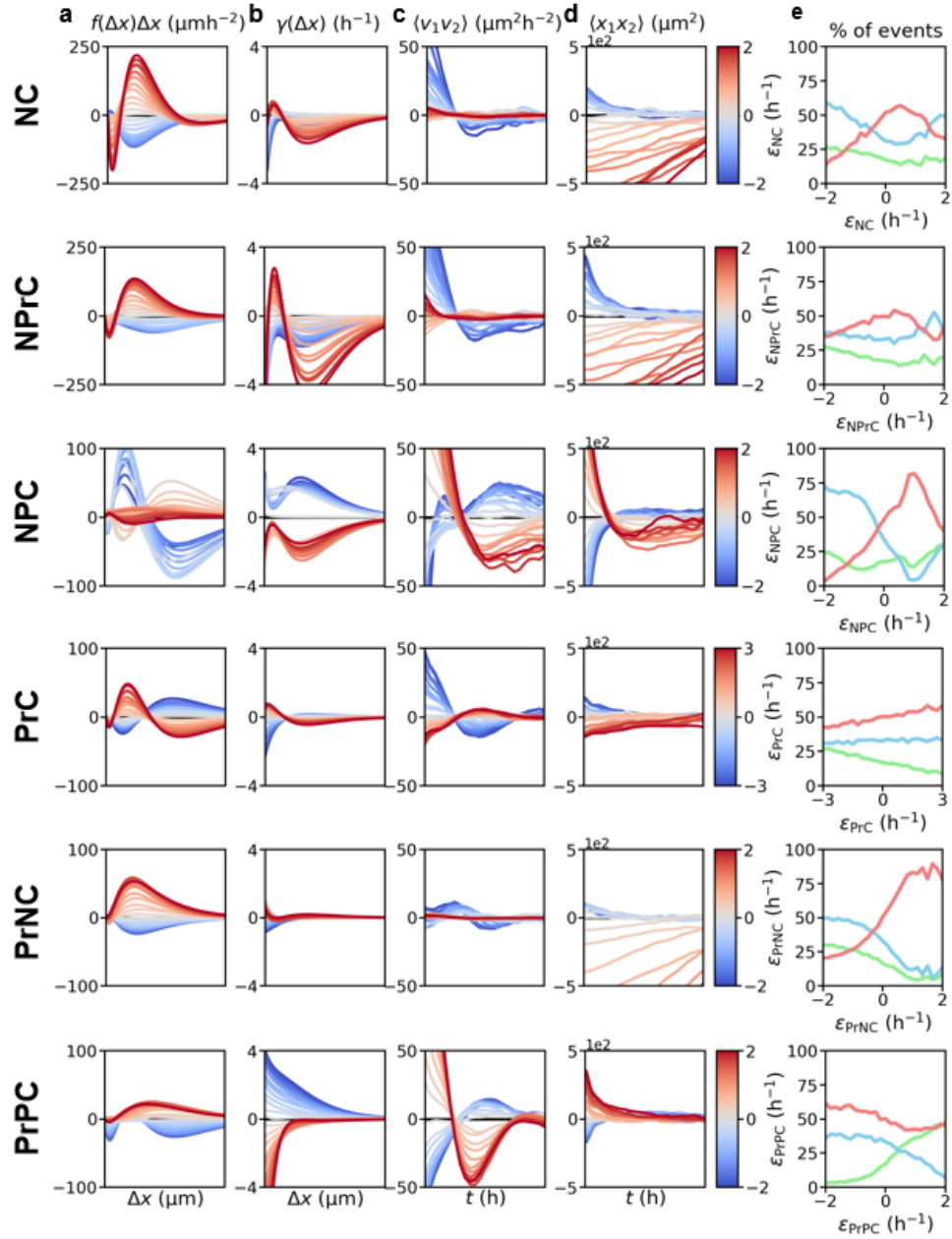


Figure S8: **Underdamped dynamics of positional candidate cell-cell interactions.** In each row, we show the underdamped dynamics of one of the positional candidate cell-cell interaction as indicated. From left to right, we show: **a)** the inferred cohesion interactions between cells, **b)** the inferred friction interactions, **c)** the velocity cross-correlation between the two cells as they are on the same island. **d)** The position correlation function between cells, characterizing the mutual exclusion behavior of cells and **e)** the collision statistics. For (a)-(d), we vary the phenomenological interaction strength as indicated on the colorbars. In (e) we vary the phenomenological interaction strength on the x-axis.

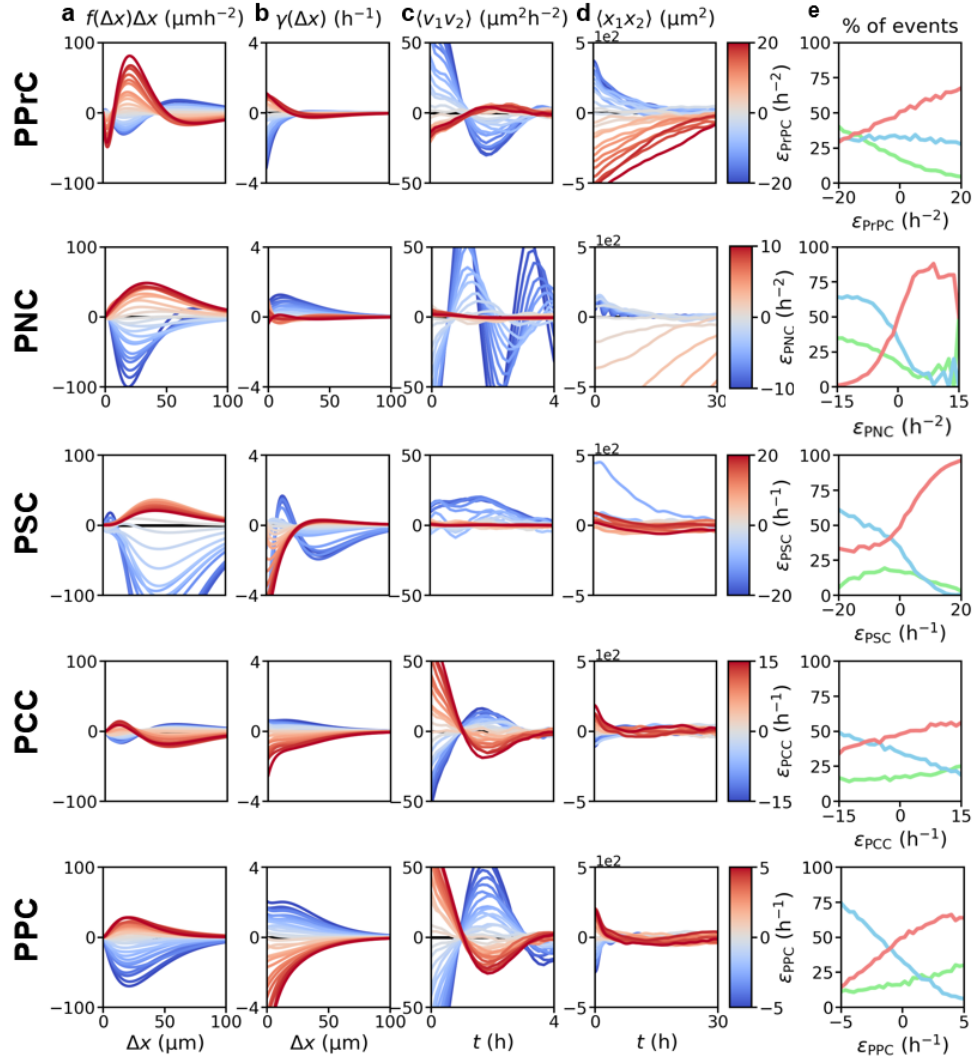


Figure S9: **Underdamped dynamics of polarity candidate cell-cell interactions.** In each row, we show the underdamped dynamics of one of the polarity candidate cell-cell interaction as indicated. From left to right, we show: **a)** the inferred cohesion interactions between cells, **b)** the inferred friction interactions, **c)** the velocity cross-correlation between the two cells as they are on the same island. **d)** The position correlation function between cells, characterizing the mutual exclusion behavior of cells and **e)** the collision statistics. For (a)-(d), we vary the phenomenological interaction strength as indicated on the colorbars. In (e) we vary the phenomenological interaction strength on the x-axis.

5.1.2 Summary of qualitative comparison of candidate cell-cell interactions

To summarize the qualitative features of our candidate cell-cell interactions, we count how many qualitative features of the two experimentally observed feature sets

- **epithelial set:** cohesion, friction, positive velocity correlations, negative position correlations, and dominant reversal behavior
- **cancer cell set:** attraction, anti-friction, negative velocity correlations, negative position correlations, and dominant sliding behavior

can be predicted by our candidate cell-cell interactions. The rules for counting are that we consider the dynamics of our candidate cell-cell interactions and then choose either positive or negative interaction strength ε to maximize the number of features our candidate cell-cell interaction can predict of a certain feature set. For example, for nucleus repulsion (NC), we see that at positive ε_{NC} , our model predicts repulsion, friction, no velocity correlations, negative position correlations, and reversal behavior. Thus, we can match 4 out of the 5 qualitative features of the epithelial feature set. For negative ε_{NC} , we find that only attraction and sliding is captured out of the cancer cell feature set. We summarize these features in table 5. Taken together, we find that only PCC and PPC can predict simultaneously 4 out of 5 qualitative features of the dynamics of both epithelial and cancer cells. These two candidate cell-cell interactions thus stand out above the other candidate cell-cell interactions as a prime candidate to provide an accurate description of the dynamics of all considered cell types. Note that PCC and PPC are mathematically very similar as both implement different versions of alignment or anti-alignment interactions. In PCC, we impose that $\dot{P}_i \sim P_j$, while in PPC, we impose that $\dot{P}_i \sim \Delta P$. Thus, in both cases, the polarity of cell i adjusts to the polarity of cell j .

candidate interaction	epithelial set	cancer cell set
nucleus repulsion	4 (repulsion, friction, exclusion, reversal)	2 (attraction, sliding)
nucleus protrusion repulsion	4 (repulsion, friction, exclusion, reversal)	1 (attraction)
nucleus polarity repulsion	3 (friction, positive vel.corr., reversal)	4 (attraction, anti-friction, negative vel.corr., sliding)
protrusion repulsion	3 (repulsion, exclusion, reversal)	2 (attraction, anti-friction)
protrusion nucleus repulsion	3 (repulsion, exclusion, reversal)	2 (attraction, sliding)
protrusion polarity repulsion	4 (repulsion, friction, positive vel.corr., reversal)	3 (attraction, anti-friction, negative vel.corr.)
polarity repulsion	3 (repulsion, exclusion, reversal)	1 (attraction)
polarity nucleus repulsion	3 (repulsion, exclusion, reversal)	4 (attraction, anti-friction, negative vel.corr., sliding)
polarity shrinking	3 (repulsion, friction, reversal)	2 (attraction, sliding)
polarity cross shrinking	4 (repulsion, friction, positive vel.corr., reversal)	4 (attraction, anti-friction, negative vel.corr., sliding)
polarity alignment	4 (repulsion, friction, positive vel.corr., reversal)	4 (attraction, anti-friction, negative vel.corr., sliding)

Table 5: Summary of the number of qualitative features that our candidate cell-cell interactions can predict out of the experimentally observed feature sets. We always find the maximum number of features that each candidate cell-cell interaction can predict at either positive or negative interaction strengths.

5.2 Quantitative fitting of the dynamics with PPC

Despite the qualitative shortcomings of some of the candidate cell-cell interactions, we nevertheless perform our quantitative fitting procedure of all candidate cell-cell interactions to the experimental data. We show the fitting performance of these fits in main text Fig. 5a,b. Here we describe in detail the

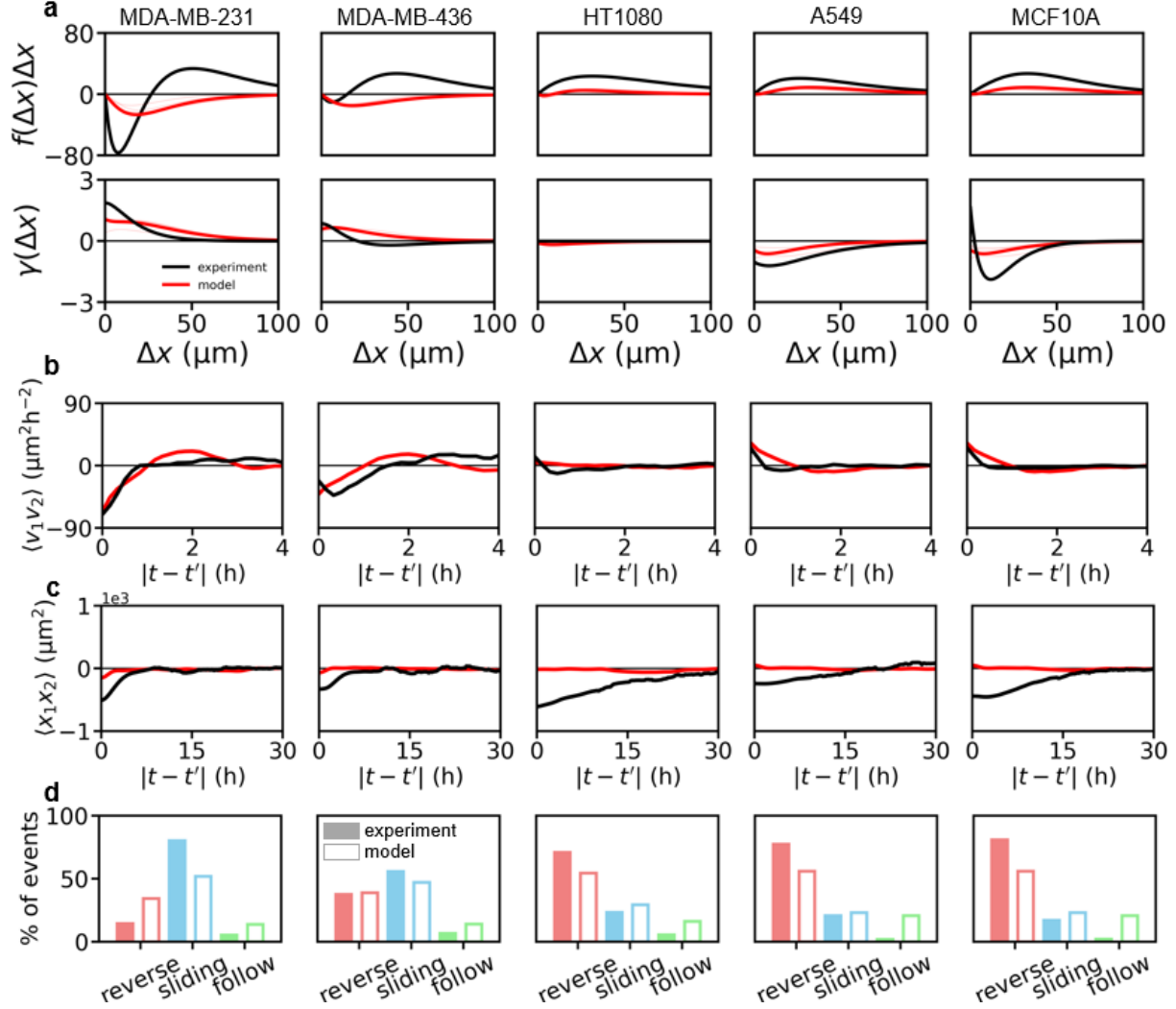


Figure S10: **Results of the global fit of only PPC to the experimental data.** **a)** Underdamped cell-cell interactions for both experiment (black) and best fitting model (red). Upper row shows the underdamped cohesion interactions, while lower row shows the inferred friction interactions. **b)-d)** All behavior statistics for both experiment (black, solid bars) and model (red, empty bars). (b) shows the velocity correlation function $\langle v_1(t)v_2(t') \rangle_{\text{same}}$ when cells are on the same island. (c) show the position correlation function $\langle x_1(t)x_2(t') \rangle$. (d) shows the collision statistics for all different cell types.

fitting result of PPC to all cell types. Corresponding to the curve in the IBS of PPC (main text Fig. 4c), PPC tunes between a combination of repulsion and friction and a combination of attraction and anti-friction. Correspondingly, PPC can capture the experimentally observed correlations of the underdamped interactions (Fig. S10a). Note however, that PPC underestimates the underdamped repulsion interactions of all cell types. Furthermore, PPC qualitatively captures the velocity cross-cross correlations and the behavior statistics (Fig. S10b,d). However, PPC underestimates for all cell types the dominant collision behavior leading to a quantitatively wrong behavior distribution. Finally, note that PPC does not predict

significant mutual exclusion behavior (Fig. S10c). This may be expected from an interaction mechanism that purely promotes anti-alignment and alignment of polarity but no interactions between polarity and cell position.

5.3 Interaction behavior arising from PPC

In this subsection, we show a detailed analysis of the dynamics arising from PPC and connect the interaction mechanism to the interaction behavior we observe in epithelial and breast cancer cell lines.

5.3.1 Polarity alignment enables reversal behavior

First, we describe how polarity alignment interactions as allowed by PPC can lead to the behavior that we observe in epithelial cells. While it is intuitive that polarity alignment promotes correlated velocities of the two cells as quantified by the velocity cross-correlation function $C_V(|t-t'|)$ ($\epsilon_{\text{PPC}} > 0$ main text Fig. 4d, 5d), the emergence of reversal behavior is more subtle. First, note that we mostly observe reversal events in our model when one cell is on an island, while the other transitions into that island ($\epsilon_{\text{PPC}} > 0$ in main text Fig. 4b, Fig. S11a). This is also typically the case for epithelial cells in the experimental data (main text Fig. 2e iv,v). Importantly, note that the behavior that we observe in our model is a result of both single cell behavior and cell-cell interactions. Specifically, note that the single cell behavior in our model yields $\langle P \rangle = 0$ when cells are on the island (equation S6). Thus, when cells collide on the island, both attain $\langle P \rangle = 0$ and the Gaussian white noise (equation S4) together with alignment interactions yield correlated fluctuating polarities (Fig. S11b) ultimately leading to correlated nucleus velocities. However, note that the cell that just transitioned into that island is located closer to the bridge (Fig. S11a). Thus,

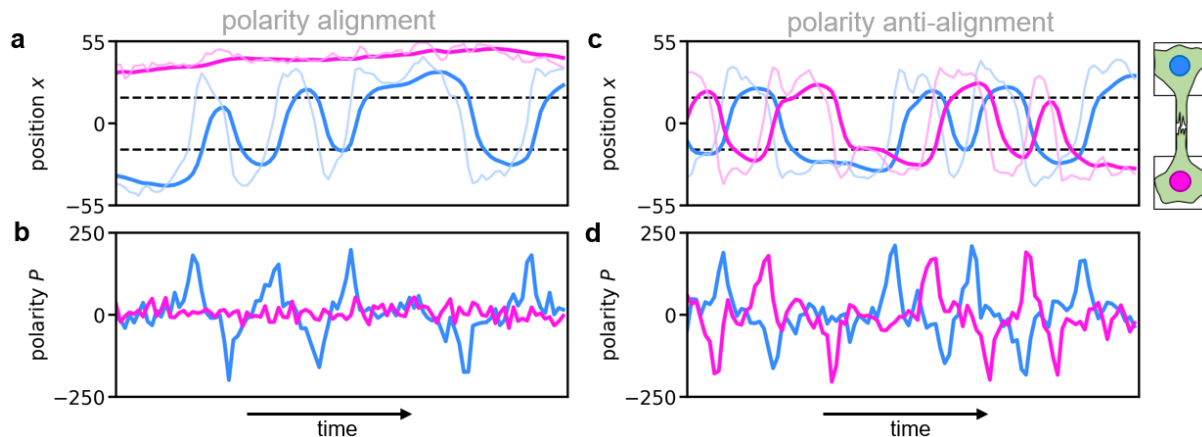


Figure S11: **Detailed dynamics of PPC** a),c) Trajectories of the two cells in space for both polarity alignment and polarity anti-alignment as allowed by PPC. Thick solid lines show the nucleus trajectories $x_n(t)$, thin faded lines show the protrusion trajectory $x_p(t)$. Horizontal dashed lines indicate the boundaries of the two islands of the dumbbell-shaped micropattern. b),d) Trajectories of the polarities $P(t)$ of the two cells.

eventually its polarity will grow into the bridge again as promoted by the positive feedback mechanisms in our model (Eqs. S4, S6), leading to reversal behavior (Fig. S11a). This illustrates that the presence of the bridge plays an important role in establishing reversal behavior of epithelial cells. Consequently, in the absence of the bridge, our model for epithelial cells shows less reversal behavior but more following behavior (Fig. S18c) as expected for polarity alignment interactions. Also in the experiment, epithe-

lial cells on rectangular patterns show more following behavior reminiscent of flocking (Fig. S18b). Taken together, this analysis illustrates that interaction behavior can be influenced by the geometry of the micropattern. However, note that cell-cell interactions themselves are not significantly affected by the geometry of the micropattern as shown in section 5.7.

Finally, note that PPC alone does not quantitatively reproduce the collision statistics of epithelial cells and overestimates following behavior (MCF10A in Fig. S10d). These following events arise from alignment interactions promoting flocking of the two cells. This may suggest that the mechanism explained above is not realistic for real cells. This is why we consider combinations of interactions as explained in section 5.5. Specifically, by combining PPC with mechanisms that also couple the polarity to the position of the cells like PPrC, we do quantitatively capture the collision behavior of epithelial cells (MCF10A in Fig. S14d). Specifically, PPrC induces growth of the polarity away from the other cell, robustly promoting reversal behavior. Thus this added CIL-like interaction may be an important component of the interaction mechanisms underlying contact-interactions between epithelial cells.

5.3.2 Polarity anti-alignment promotes sliding behavior

Next, we describe the sliding dominated dynamics arising from anti-alignment. First, it is intuitive that anti-alignment leads to both anti-correlated velocities and sliding behavior ($\epsilon_{\text{PPC}} < 0$ main text Fig. 4d,f and Fig. 5d,f). Interestingly, we mostly observe sliding behavior in our model while cells transition between the two islands ($\epsilon_{\text{PPC}} < 0$ in main text Fig. 4b, Fig. S11c). Again, this is a feature we observe for breast cancer cells in our experiment (main text Fig. 2e i,ii). In our model, this happens because as one cell starts to transition, its polarity grows towards the bridge. Consequently, when the other cell is on the opposite island, polarity anti-alignment leads to growth of the polarity of that other cell into the bridge as well. (Fig. S11d). This yields almost simultaneous transitions of both cells including sliding behavior during the transition.

5.4 Constraining power of inferred interactions

For our fitting procedure it is important that inferred interactions and experimental behavior statistics are effectively independent statistics given our phenomenological model. To test this, we perform our fitting procedure while considering different total coefficients of determination (COD). Specifically, before, we averaged the different CODs of the various behavior statistics and inferred cell-cell interactions to reach a good fit for all the considered quantities (equation S13). Now, we fit these quantities separately. This allows us to disentangle the effect of individual quantities on the resulting fit. We consider two cases:

1. Only behavior statistics: $R_k^2 = \frac{1}{2} (R_{v,k}^2(\Theta) + R_{c,k}^2(\Theta))$
2. Only inferred interactions: $R_k^2 = R_{d,k}^2(\Theta)$

If the behavior statistics are really effectively independent of the inferred interactions in our phenomenological model, we would expect that both cases should give different final fitting results. Specifically, we would expect that the optimum $\hat{\mathcal{R}}^2$ is reached at different parameters Θ and/or the value of $\hat{\mathcal{R}}^2$ is different between the two cases. Both of these cases are generally true for the global fit and all candidate cell-cell interactions. Specifically, we consider for the best fitting candidate cell-cell interaction

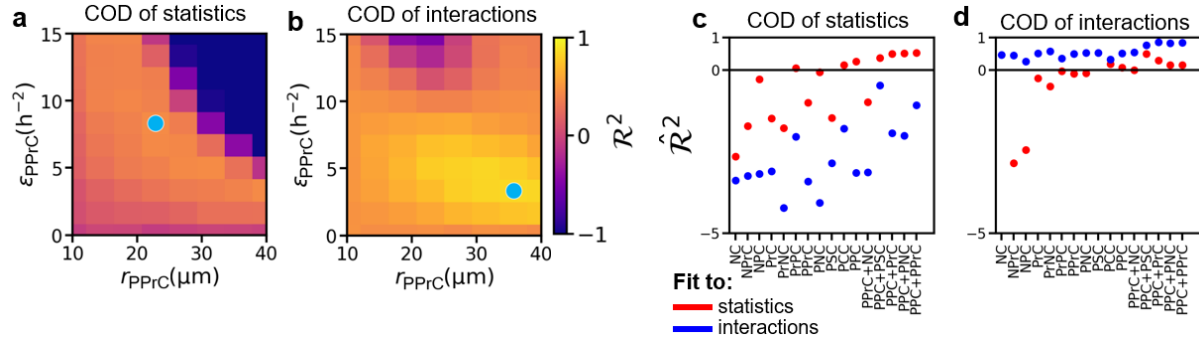


Figure S12: **Constraining power of inferred underdamped cell-cell interactions.** **a)-b)** Coefficient of determination $\mathcal{R}^2(r)$ as determined in equation S18 for the candidate cell-cell interaction PPC+PPrC. Panel (a) shows the COD for capturing only the statistics as defined in case 1. Panel (b) shows the COD for capturing only the inferred underdamped cell-cell interactions as in case 2. Blue dots indicate the optimum reached for all of these two cases. **c)-d)** Maximum COD for all candidate cell-cell interaction as defined in equation S20. Again we consider the two different cases of only fitting the statistics (red) or only interactions (blue). For each of these cases, we find the maximum COD that we can reach with fitting different quantities.

PPC+PPrC the two cases as defined above. Then, after performing the global fitting procedure, we compute $\mathcal{R}^2(\epsilon_{\text{PPPrC}}, r_{\text{PPPrC}})$ and find that this global COD has optima at different values for ϵ_{PPPrC} and r_{PPPrC} in the two different definitions for the COD (Fig. S12a,b). This means that only fitting the behavior statistics will yield different final parameters than fitting only the inferred underdamped interactions. Furthermore, we consider for all candidate cell-cell interactions the maximum values of $\mathcal{R}^2(\epsilon_{\text{PPPrC}}, r_{\text{PPPrC}})$, which we defined as $\hat{\mathcal{R}}^2$ in equation S20 and showed in main text Fig. 5b. Again, we consider the two different cases defined above. For all the definitions for $\hat{\mathcal{R}}^2$, we perform the global fit and then separately assess how well the statistics and the inferred interactions are captured (Fig. S12c,d). We find that if we fit only the behavior statistics, as expected, the behavior statistics are well captured. However, the inferred interactions are not in this case (red dots in Fig. S12c,d). In contrast, if we fit the inferred interactions, these interactions are well captured while the behavior statistics are not (blue dots in Fig. S12c,d). Thus, taken together, these results reveal that in our phenomenological model for all candidate cell-cell interaction, the inferred cell-cell interactions are an effective independent statistics in addition to the behavior statistics. This shows that including the inferred cell-cell interactions does indeed provide additional strong constraints on the phenomenological model. Throughout this paper, we define: $R_k^2 = (\frac{1}{2}R_{d,k}^2(\Theta) + \frac{1}{4}R_{v,k}^2(\Theta) + \frac{1}{4}R_{c,k}^2(\Theta))$. This definition puts equal weight on all quantities. Note that $R_{d,k}^2(\Theta)$ already is the COD of both the underdamped cohesion and underdamped friction interactions.

5.5 Combining candidate cell-cell interactions

To potentially overcome the shortcomings of our single candidate cell-cell interactions, we test combinations of the various different candidate interactions. Specifically, as we observe that PPC on its own already provides in general the best fit of the dynamics of the various different cell types, we consider combinations of PPC and one of the other candidate interactions.

5.5.1 Underdamped dynamics of combined interactions

Prime candidates to combine with PPC are interactions that add effective repulsion to the dynamics and generate mutual exclusion behavior. These are features of NC, NPrC, PrC, PPrC, or PNC with $\varepsilon > 0$ (Fig. S8, Fig. S9). Furthermore, we observed that PPC can not well capture the dynamics of HT1080 cells. Thus, using either PrC, PrNC, PPrC, or PNC could allow us to also capture the dynamics of these cells. For instance, combining PPC with PPrC has an interesting effect on the dynamics of polarity alignment interactions: While the underdamped repulsion interactions increase, the underdamped friction interactions get weaker (Fig. S13ai,ii). Furthermore, the velocity correlations get weaker, while the position correlation functions get increasingly negative (Fig. S13aiii,iv). These changes indicate that additional repulsion interactions in the form of PPrC weakens the coordination of the two cells but increases the mutual exclusion behavior. Finally, additional PPrC leads to more reversal behavior (Fig. S13av). In contrast, for polarity anti-alignment, we find that additional polarity repulsion (PPrC) qualitatively changes the dynamics and introduces long range repulsion to the attractive interactions of polarity alignment (Fig. S13bi). Furthermore, the effect on the inferred underdamped friction interactions, velocity correlations, position correlations, and collision statistics are similar to that of the case with polarity alignment (Fig. S13bii-iv). Thus, additional PPrC can remedy the shortcomings of PPC discussed above: PPrC adds underdamped repulsion interactions, leads to stronger mutual exclusion behavior and increases the percentage of observed reversal behavior for alignment. Consequently, the combined model can better fit the experimental data of epithelial and breast cancer cells (main text Fig. 5a, Fig. S15,S14).

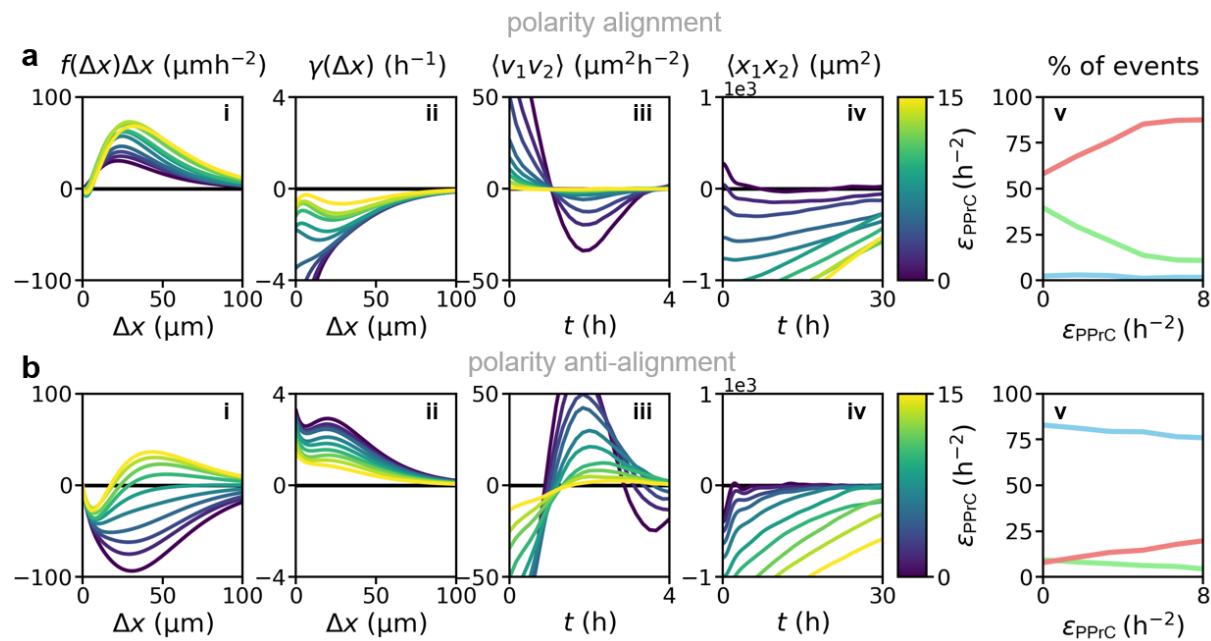


Figure S13: **Dynamic effects of polarity repulsion on polarity alignment.** a) Underdamped dynamics and behavior statistics of the combined candidate cell-cell interactions PPC+PPrC. We show how the dynamics and behavior statistics change when we fix the polarity alignment strength ε_{PPC} and the two interaction ranges r_{PPC} and r_{PPrC} while varying the strength of the additional repulsion interaction ε_{PPrC} . Panel (a) shows polarity alignment ($\varepsilon_{PPC} = 4.3$), panel (b) shows polarity anti-alignment ($\varepsilon_{PPC} = -3.9$)

5.5.2 Other combinations without PPC

Finally, note that the improved performance of combinations of PPC and other interactions is not merely the consequence of including more parameters in the fit. Instead, our results suggest that including PPC in the combination is necessary to reach good fitting performance. We show this by also considering the combination of PPrC with NC. This combination does not provide a significantly improved fit compared to only using PPrC (main text Fig. 5a).

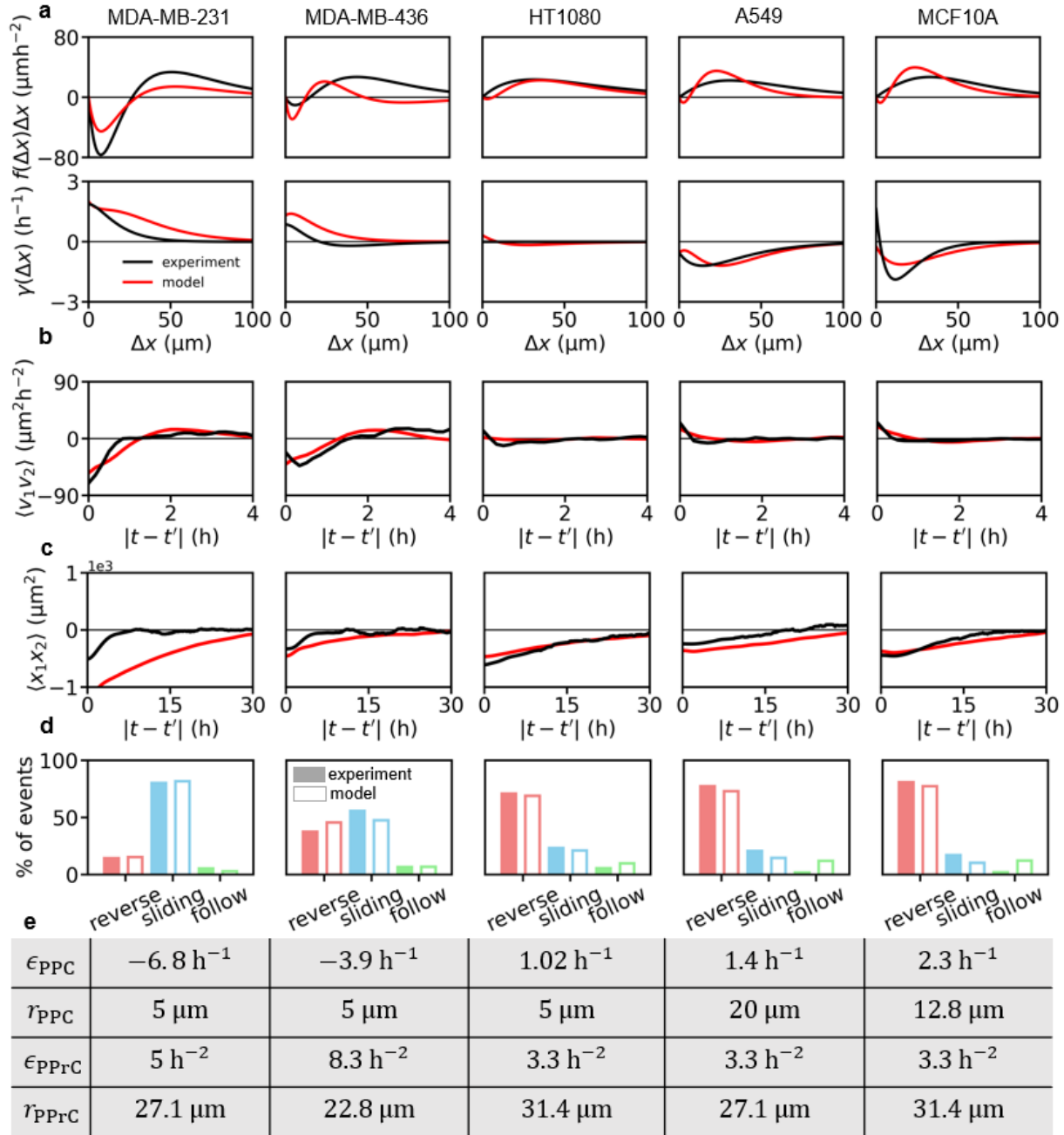


Figure S14: **Results of individual fit of PPC+PPrC to the experimental data.** **a)** Underdamped cell-cell interactions for both experiment (black) and best fitting model (red). Upper row shows the underdamped cohesion interactions, while lower row shows the inferred friction interactions. **b)-d)** All behavior statistics for both experiment (black, solid bars) and model (red, empty bars). (b) shows the velocity correlation function $\langle v_1(t)v_2(t') \rangle_{\text{same}}$ when cells are on the same island. (c) show the position correlation function $\langle x_1(t)x_2(t') \rangle$. (d) shows the collision statistics for all different cell types. **e)** Table shows the final best fitting parameters for the model PPC+PPrC for all the different cell types.

5.5.3 More than two interaction mechanisms

In this subsection, we assess whether adding a third interaction mechanism provides an improved fit of the experimental data compared to our best performing combination of PPC and PPrC. Considering

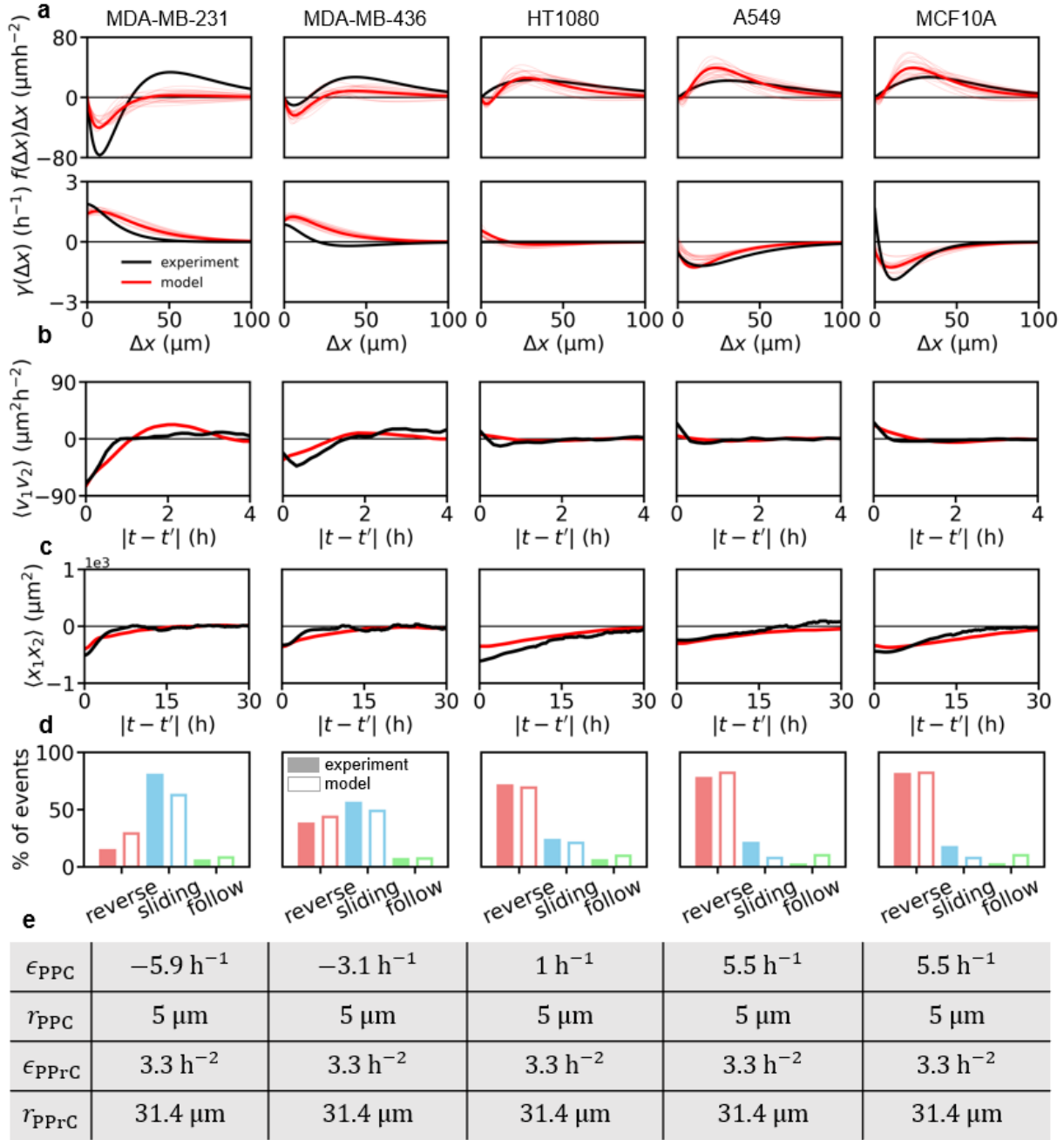


Figure S15: **Results of the global fit of PPC+PPrC to the experimental data.** **a)** Underdamped cell-cell interactions for both experiment (black) and best fitting model (red). Upper row shows the underdamped cohesion interactions, while lower row shows the inferred friction interactions. **b)-d)** All behavior statistics for both experiment (black, solid bars) and model (red, empty bars). (b) shows the velocity correlation function $\langle v_1(t)v_2(t') \rangle_{\text{same}}$ when cells are on the same island. (c) show the position correlation function $\langle x_1(t)x_2(t') \rangle$. (d) shows the collision statistics for all different cell types. **e)** Table shows the final best fitting parameters for the model PPC+PPrC for all the different cell types. In the global fit, we only allow ϵ_{PPC} to vary across distinct cell types.

three candidate interactions simultaneously is computationally very expensive. Thus, we consider here an example triplet consisting of PPC, PPrC and NC. Here, NC stand for nucleus coupling allowing for nucleus repulsion or attraction. Such an interaction is potentially critical as the nucleus of cells may

contribute crucial excluded volume interactions. To assess whether this third interaction improves the fitting performance, we aim to find the global coefficient of determination $\mathcal{R}(\varepsilon_{\text{PPrC}}, \varepsilon_{\text{NC}}, r_{\text{PPC}}, r_{\text{PPrC}}, r_{\text{NC}})$ as defined in equation S18. However, as this is numerically costly, we vary only simultaneously the interaction strengths of all three interaction mechanisms ε_{PPC} , $\varepsilon_{\text{PPrC}}$, and ε_{NC} . In this procedure, we fix the interaction ranges r_{PPC} and r_{PPrC} to the optimal values found through the global fit of PPC and PPrC as described in section 4.5.2. We set the interaction range to $r_{\text{NC}} = 10\mu\text{m}$ and $r_{\text{NC}} = 30\mu\text{m}$. We thus compute the global coefficient of determination $\mathcal{R}(\varepsilon_{\text{PPrC}}, \varepsilon_{\text{NC}})$, which we depict in Fig. S16a,b. We find that $\mathcal{R}(\varepsilon_{\text{PPrC}}, \varepsilon_{\text{NC}})$ is maximized when $\varepsilon_{\text{NC}} \simeq 0$ independent of r_{NC} . This procedure cannot exclude new maxima in the full coefficient of determination $\mathcal{R}(\varepsilon_{\text{PPrC}}, \varepsilon_{\text{NC}}, r_{\text{PPC}}, r_{\text{PPrC}}, r_{\text{NC}})$. However, our analysis shows that the maximum we found in $\mathcal{R}(\varepsilon_{\text{PPrC}}, r_{\text{PPC}}, r_{\text{PPrC}})$ in the global fit of PPC and PPrC is at least a local maximum in the more complex $\mathcal{R}(\varepsilon_{\text{PPrC}}, \varepsilon_{\text{NC}}, r_{\text{PPC}}, r_{\text{PPrC}}, r_{\text{NC}})$. This indicates that the best fitting parameter combination of PPC and PPrC can not be gradually improved by adding additional nucleus coupling.

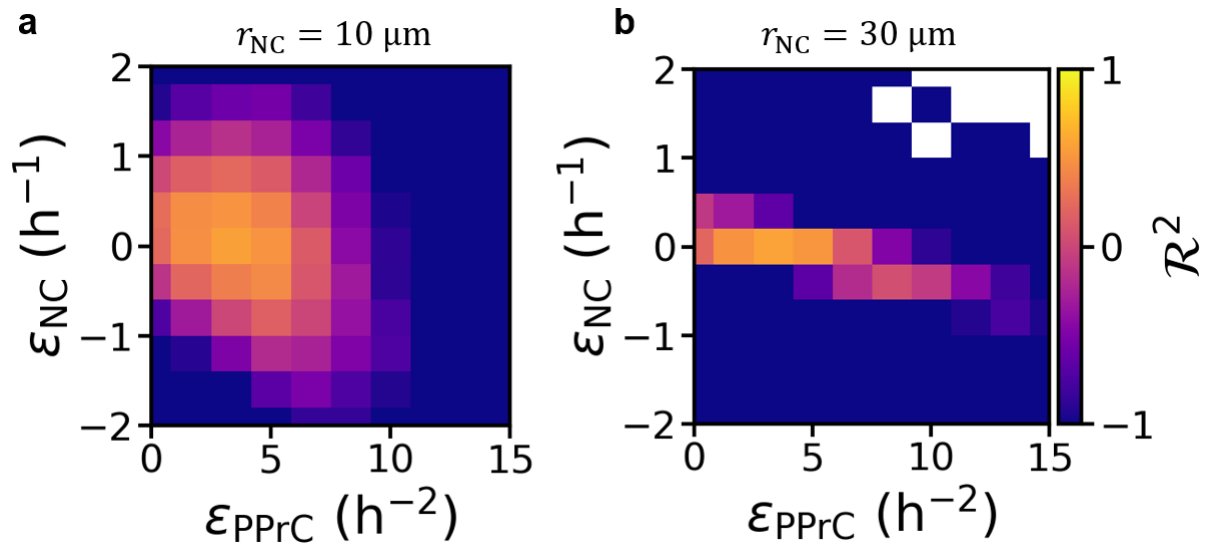


Figure S16: **Global fit of three interaction mechanisms a),b)** Global coefficient of determination $\mathcal{R}(\varepsilon_{\text{PPrC}}, \varepsilon_{\text{NC}})$ for a model with the three interaction mechanisms PPC, PPrC and NC. Panel (a) shows \mathcal{R} at $r_{\text{NC}} = 10\mu\text{m}$, panel (b) at $r_{\text{NC}} = 30\mu\text{m}$. The maximum is located near $\varepsilon_{\text{NC}} = 0$ indicating that NC does not improve the fitting performance of the best fitting parameter combination of the model with only PPC and PPrC.

5.6 The role of single cell behavior

In this section, we study the role of the single cell terms in our phenomenological model. Specifically, in the absence of cell-cell interactions, our model is consistent with the mechanistic model for MDA-MB-231 cells used in [3]. Given that we here study multiple different cell lines, it is a key question whether the single cell dynamics of our model has a significant impact on the results about cell-cell interactions presented in the main text.

To answer this question, we first determine the range of single cell parameters that is relevant to describe single cell behavior observed in our experiments. Therefore, we find the best single cell parameters for a second cell line, which is significantly different from MDA-MB-231 cells. A prime candidate are MCF10A cells as they show a slightly lower probability to be on the bridge and a significantly higher survival probability (Fig. S2d i,v). To capture the different single cell features of MCF10A cells, we vary

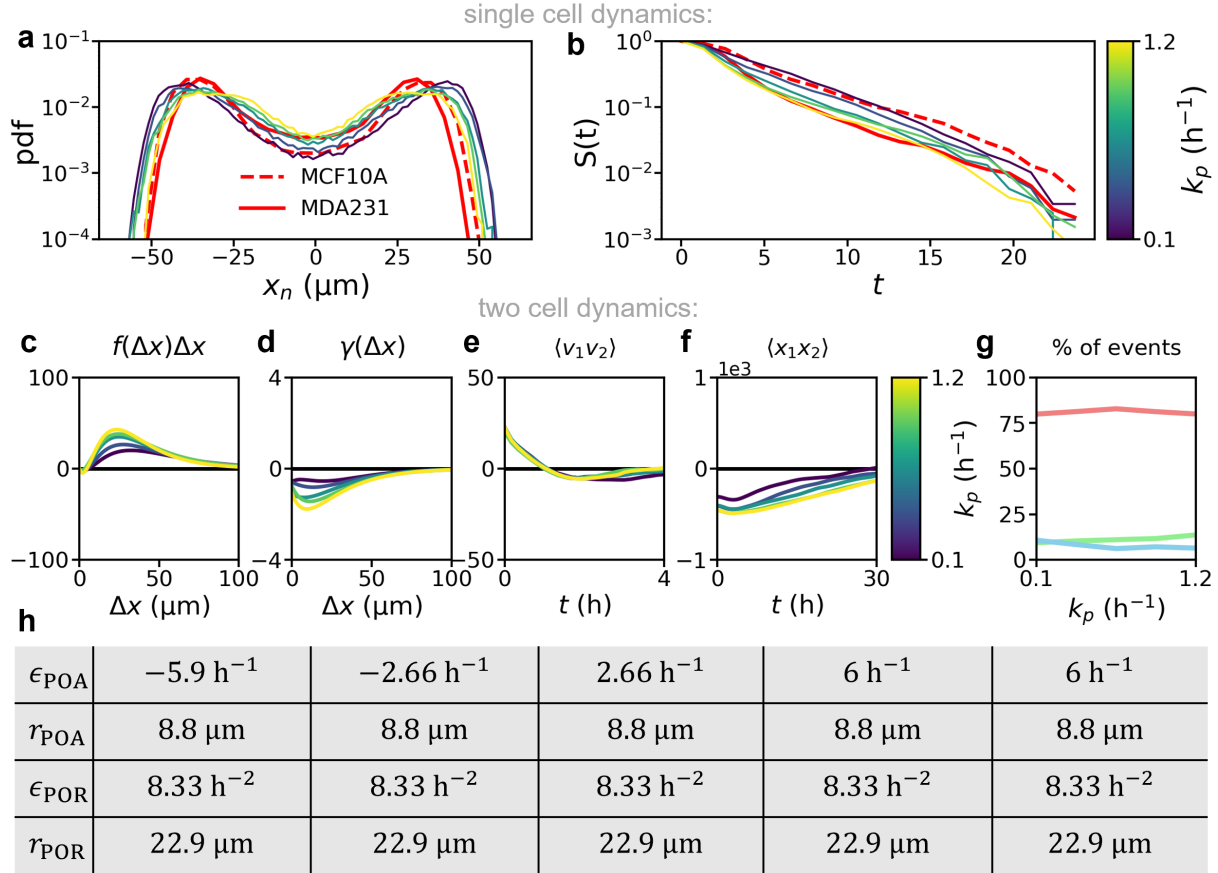


Figure S17: Influence of single cell dynamics on two cell dynamics. **a)** Distribution of nucleus positions for both model and experiment (red) for model and experiments of a single cell on the dumbbell-shaped micropattern. Red solid line shows the experimental result of MDA-MB-231 cells and red dashed line indicates MCF10A cells. Colored lines indicate model results and colorbar for varying k_p is located next to panel b. **b)** Survival probability of both model (colored) and experiment (red) for single cells on the pattern. Legend of panel a applies also here. **c)-g)** Model predictions for the two-cell dynamics dependent on the single cell parameter k_p . Panel (c) shows the underdamped repulsion interactions, panel (d) shows the underdamped friction interactions, panel (e) shows the velocity cross-correlation of two cells on the same island. Panel (f) shows the position correlations of the two cells. Colorbar in panel f applies to panels c-f. Panel (g) shows the percentage of each type of collision event dependent on k_p . **h)** Resulting parameters in our phenomenological model after globally fitting the dynamics of cell-cell interactions.

key single cell parameters in our phenomenological model. Specifically, the reduced spring constant $k_p = k/\zeta_p$ (equation S3) determines how the protrusion of a cell responds to the nucleus position. We find that k_p influences the probability distribution of the nucleus positions and sets the survival probability of single cells (Fig. S17a,b). Decreasing k_p from 1.2 h^{-1} for MDA-MB-231 cells to a value of around 0.1 h^{-1} allows us to capture the reduced probability of cells being on the bridge and enables us to capture the higher survival probabilities of MCF10A cells. Importantly, this different single cell behavior does not greatly influence the inferred underdamped cell-cell interactions and behavior statistics predicted by our phenomenological model (Fig. S17c-g). Nevertheless, we repeat our quantitative fitting procedure with the different single cell parameters for MCF10A cells instead of the single cell parameters of the MDA-MB-231 cells. We find that the best fitting interaction parameters in our phenomenological model are only mildly affected by the different single cell behavior (Compare Fig. S17h to Fig. S15e). Thus, for the sake of simplicity, we opt to keep the single cell behavior constant throughout this study, knowing that the single cell behavior does not qualitatively influence the dynamics emerging from cell-cell

interactions. This is supported by the observation that almost all our cells obey qualitatively very similar underdamped single cell dynamics (Fig. S2e).

5.7 Polarity-polarity coupling on rectangular patterns

To test whether insights of our phenomenological model sensitively depend on the chosen dumbbell-shaped geometry of our micropattern, we additionally investigate cell-cell interactions on rectangular micropatterns (Fig. S18a). Specifically, we consider the epithelial cell line MCF10A and the breast cancer cell line MDA-MB-231 and track cell nuclei (Fig. S18b). We first infer the underdamped cell-cell interactions for these two cell types on the rectangular pattern and compare our results to the inferred underdamped cell-cell interactions on the dumbbell-shaped micropattern. For MCF10A cells, we find that these cells obey qualitatively similar underdamped cell-cell interactions on both geometries (black and grey curves in Fig. S18d,e). However, the underdamped cohesion interactions are weaker on the rectangular pattern. Furthermore, in agreement with previous work [1], MDA-MB-231 cells exhibit quantitatively similar underdamped cell-cell interactions (black and grey curves in Fig. S18g,h). These results show that the geometry of the micropattern has only minor impact on the inferred underdamped cell-cell interactions.

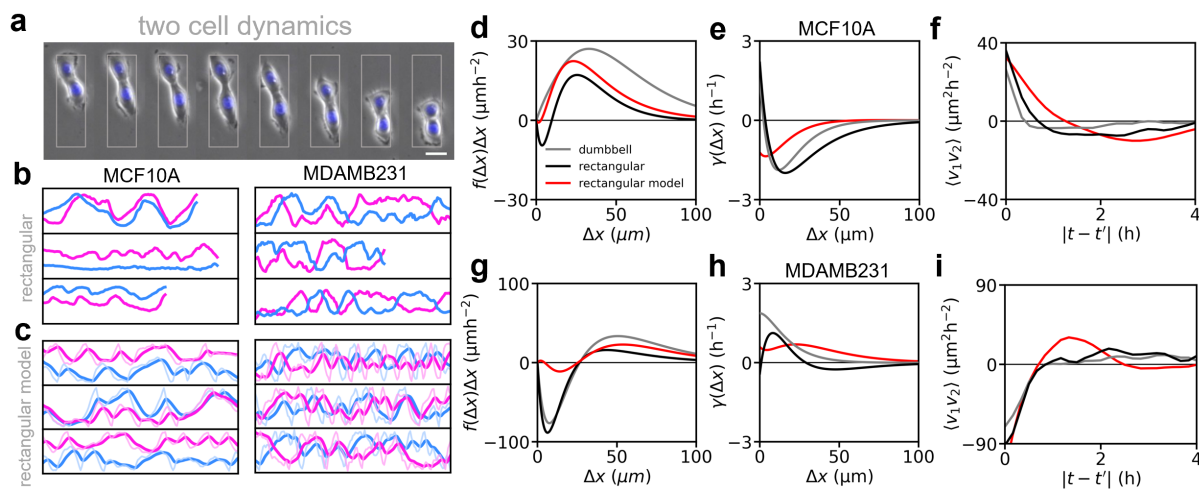


Figure S18: **Alignment interactions on rectangular patterns.** **a)** Time series of brightfield images of two MCF10A cells interacting on a rectangular micropattern. Scale bar: $25 \mu\text{m}$. **b)** Sample of cell trajectories obtained from our experiments on a rectangular pattern for both MCF10A and MDA-MB-231 cells. **c)** Sample of trajectories predicted by our phenomenological model with PPC+PPrC as cell-cell interaction. **d)-e)** Inferred underdamped cohesion interactions (d), inferred underdamped friction interactions (e), and velocity cross-correlation function of two MCF10A cells for the dumbbell pattern (grey), the rectangular pattern (e), and the phenomenological model fitted to the rectangular dynamics (red). **g)-i)** Inferred underdamped cohesion interactions (g), inferred underdamped friction interactions (h), and velocity cross-correlation function of two MDA-MB-231 cells for the dumbbell pattern (grey), the rectangular pattern (e), and the phenomenological model fitted to the rectangular dynamics (red).

To test whether our phenomenological model can also capture the two-cell dynamics on a rectangular pattern, we perform numerical simulations of our phenomenological model on this alternative geometry. Specifically, we consider the best fitting candidate cell-cell interaction PPC+PPrC and use for both MCF10A and MDA-MB-231 cells the best interaction parameters obtained from our global fit on the

dumbbell pattern (Fig. S15e). Importantly, in order to capture the dynamics on a different geometry, we have to adjust the single cell aspects of our phenomenological model: We need to remove the geometry dependence of the single cell terms in our phenomenological model (equations S5 and S6), which implemented the adaptation of the cell's migratory machinery to the confinement of the bridge in our dumbbell-shaped micropattern [3]. Specifically, we set $\gamma(x_n) = 1$ and $\alpha(x_p) = \alpha_0$. We analyze single cells migrating on rectangular pattern to constrain single cell parameters in our model (Fig. S19). We find that to best capture the dynamics of the cells on the rectangular pattern, we have to set α_0 to negative values such that cells remain polarized on the rectangular pattern. We choose $\alpha_0 = -0.3$. To better capture experimental trajectories of single cells on rectangular patterns, we also change the values of σ and k_n . Specifically, for MCF10A cells, we choose $\sigma = 40$ and $k_n = 1.2$. These two changes are necessary to capture the high persistence and frequent turn around events of our MCF10A cells on the rectangular pattern (Fig. S19a) as also quantified by a velocity auto-correlation function $\Phi(t) = \langle v(t')v(t+t') \rangle_{t'}$ (Fig. S19b). Physically, increasing k_n means that we couple the nucleus closer to the protrusion. This change may be in agreement with the observation of reduced elongation of the cells on rectangular patterns compared to the dumbbell shaped patterns (Fig. S18a, SI movie). On the rectangular patterns, we observe that when cells hit one of the ends of the rectangular pattern, they polarize away from the end and turn around. We implement this by including a boundary condition where the polarity P of a cell gets flipped to $-P$ as soon as cells hit the boundary of our pattern. For MDA-MB-231 cells, we increase σ to $\sigma = 150$ to capture the higher stochasticity of the single cell behavior of these cells on the rectangular pattern (Fig. S19c,d).

Having constrained the single cell parameters, we can now simulate our phenomenological model on a rectangular pattern. We find that using the interaction parameters best describing the dynamics on the dumbbell-shaped geometry, also yields a good description of the dynamics on the rectangular geometry. Specifically, we can qualitatively capture the flocking and frequent reversal behavior of MCF10A cells on the rectangular pattern (Fig. S18b,c). Furthermore, our phenomenological model qualitatively captures the inferred interactions (Fig. S18d,e) and the positive velocity correlations of MCF10A cells on the rectangular pattern (Fig. S18f). Moreover, our model captures the frequent sliding events of MDA-MB-231 cells (Fig. S18b,c) as well as qualitatively the short timescale dynamics of these cells (Fig. S18g-i). Taken together, these results show that our phenomenological model can be generalized to a different geometry. Thus, the identified polarity-polarity coupling interactions do not depend on the specific dumbbell-shaped geometry used in the main text.

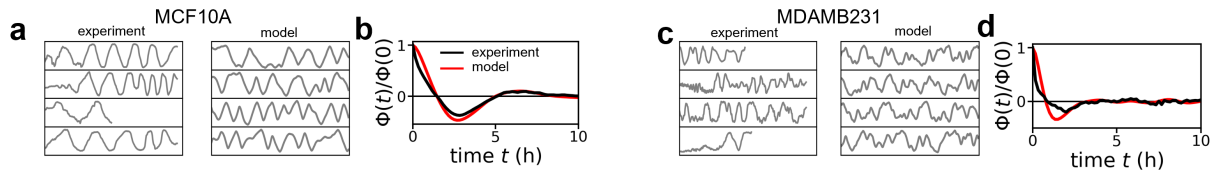


Figure S19: **Single cell dynamics on rectangular patterns.** **a)** Sample of cell trajectories of a single MCF10A cell on a rectangular pattern for both experiment and model. **b)** Velocity auto-correlation function of MCF10A cells on rectangular pattern for both experiment (black) and model (red). **c)** Sample of cell trajectories of a single MDA-MB-231 cell on a rectangular pattern for both experiment and model. **d)** Velocity auto-correlation function of MDA-MB-231 cells on rectangular pattern for both experiment (black) and model (red).

Supplementary References

- [1] Brückner DB, Arlt N, Fink A, Ronceray P, Rädler JO, Broedersz CP. 2021 Learning the dynamics of cell–cell interactions in confined cell migration. *Proc. Natl. Acad. Sci. U. S. A.* **118**, 7. (doi:10.1073/pnas.2016602118).
- [2] Brückner DB, Fink A, Schreiber C, Röttgermann PJ, Rädler JO, Broedersz CP. 2019 Stochastic nonlinear dynamics of confined cell migration in two-state systems. *Nat. Phys.* **15**, 6, 595–601. (doi:10.1038/s41567-019-0445-4).
- [3] Brückner DB, Schmitt M, Fink A, Ladurner G, Flommersfeld J, Arlt N, Hannezo E, Rädler JO, Broedersz CP. 2022 Geometry Adaptation of Protrusion and Polarity Dynamics in Confined Cell Migration. *Phys. Rev. X* **12**, 3, 31041. (doi:10.1103/PhysRevX.12.031041).
- [4] Flommersfeld J, Stöberl S, Shah O, Rädler JO, Broedersz CP. 2024 Geometry-Sensitive Protrusion Growth Directs Confined Cell Migration. *Phys. Rev. Lett.* **132**, 9, 98401. (doi:10.1103/PhysRevLett.132.098401).
- [5] Brückner DB, Ronceray P, Broedersz CP. 2020 Inferring the Dynamics of Underdamped Stochastic Systems. *Phys. Rev. Lett.* **125**, 5. (doi:10.1103/PhysRevLett.125.058103).
- [6] Bertrand T, D’Alessandro J, Maitra A, Jain S, Mercier B, Mège RM, Ladoux B, Voituriez R. 2024 Clustering and ordering in cell assemblies with generic asymmetric aligning interactions. *Phys. Rev. Res.* **6**, 2, 34–38. (doi:10.1103/PhysRevResearch.6.023022).